

Prediction of numerical homogenization using deep learning for the Richards equation

Sergei Stepanov^a, Denis Spiridonov^a, Tina Mai^{b,c,*}

ABSTRACT. For the nonlinear Richards equation as an unsaturated flow through heterogeneous media, we build a new coarse-scale approximation algorithm utilizing numerical homogenization. This approach follows deep neural networks (DNNs) to quickly and frequently calculate macroscopic parameters. More specifically, we train neural networks with a training set consisting of stochastic permeability realizations and corresponding computed macroscopic targets (effective permeability tensor, homogenized stiffness matrix, and right-hand side vector). Our proposed deep learning scheme develops nonlinear maps between such permeability fields and macroscopic characteristics, and the treatment for Richards equation's nonlinearity is included in the predicted coarse-scale homogenized stiffness matrix, which is a novelty. This strategy's good performance is demonstrated by several numerical tests in two-dimensional model problems, for predictions of the macroscopic properties and consequently solutions.

Keywords. Numerical homogenization; Deep learning; Nonlinear Richards equation

Mathematics Subject Classification 2020. 65M60, 65M12, 68T07

Sergei Stepanov; ^aLaboratory of Computational Technologies for Modeling Multiphysical and Multiscale Permafrost Processes, North-Eastern Federal University, 677000 Yakutsk, Republic of Sakha (Yakutia), Russia; cepe2a@inbox.ru

Denis Spiridonov; ^aLaboratory of Computational Technologies for Modeling Multiphysical and Multiscale Permafrost Processes, North-Eastern Federal University, 677000 Yakutsk, Republic of Sakha (Yakutia), Russia; d.stalnov@mail.ru

*Corresponding author: *Tina Mai*; ^bInstitute of Research and Development, Duy Tan University, Da Nang, 550000, Vietnam; ^cFaculty of Natural Sciences, Duy Tan University, Da Nang, 550000, Vietnam; maitina@duytan.edu.vn

Date: August 26, 2022.

1. INTRODUCTION

Unsaturated flow happens in soils when soil water travels downward, the topsoil dries out due to evaporation, or water permeates the soil surface across many soils' pores [35, 50]. This generally leads to the conception of soil moisture [50], described by water content (the amount of water in unsaturated soils) and water potential (the water's energy state). Despite being a minor component of the water cycle, soil moisture is necessary for a number of hydrological, biological, and biogeochemical processes. For instance, soil moisture is a crucial factor in agronomy, environmental management, sanitary engineering, groundwater storage, weather prediction, balances of energy, earth's dynamic systems, etc. The related procedures are mathematically modeled by the Richards equation [40, 4, 3, 19, 13], depicting how water moves through unsaturated soil surface that is filled with both water and air [9, 50].

In this paper, the Richards equation is considered in non-periodic and heterogeneous media. Obstacles further develop when there are material property uncertainties in some local areas, which are typical for subsurface activities, oil reservoirs, infiltration, aquifers, and most real-world simulation models. The variability of such properties' uncertainty is usually spatial.

Traditional direct methods can solve those problems in a few steps using fine-grid simulation. First, a local fine grid is built. The equation is then discretized on that fine grid, and the set of local solutions is utilized to form a global solution. This approach can be operated with well-known frameworks like the Finite Element Method (FEM) [2] and the Finite Volume Method (FVM). The grid size needs to be as small as possible to explicitly resolve all grid-level heterogeneity in order for it to be applicable and to achieve convergence. However, the smaller the grid size is, the larger the computing resources are demanded. Hence, some sort of model reduction is required. Familiar techniques involve dividing the focused domain into coarse-scale grid blocks and then calculating the effective coefficients in each coarse block [10]. This computation needs the local problems' fine-scale solutions in each coarse-grid cell or representative volume (in conventional upscaling approaches based on homogenization, whose expansion can be used to derive multicontinuum methods in a new article [11]). For our case of non-periodic media, numerical homogenization [5] is applied to single-continuum Richards equation. Concerning approximation on a macroscale computational grid, homogenization assumes that local problems' solutions carry microscale information.

Given largely different permeability fields' realizations, the computing effort can become enormous. Therefore, establishing a functional link between the permeability fields and the local macroscopic coefficients can prevent the need for repeated, costly calculations and so significantly alleviate the computational complexity. Because of various media properties, such a functional relationship is nonlinear and thus usually needs high-order approximations when modelling. Consequently, utilizing machine learning techniques to create these complicated models is natural [51, 12].

Deep neural networks (DNNs) fall under the machine learning framework [34], which constitutes a type of artificial intelligence. In this research, we use DNNs to investigate numerical homogenization. A deep neural network's structure is often made up of numerous layers, each of which contains several neurons (as nonlinear processing units for

extracting features) [28]. Right after the input layer, the first hidden layer of a deep neural network (DNN) learns basic characteristics, which are then supplied to the second hidden layer, for training itself to identify increasingly complex and abstract properties. This architecture continues on succeeding levels as the layers build up until the output is accurate enough to be considered acceptable. To enhance the expressive capability of neural networks, some nonlinear activation functions (such as ReLU, sigmoid, and tanh) are required between layers, from an input neuron to an output neuron. The output is then sent into the network's next layer as an input. Recently, deep neural networks have been effectively applied to problems needing pattern recognition, including picture identification, voice recognition as well as processing of natural language, and have been used to comprehend complex data sets [27, 23, 20]. Additionally, extensive study has been carried out to examine the descriptive potential of deep neural networks [8, 24, 43, 34, 18]. There is a variety of other applications employed DNN [47, 53, 52, 6] and convolutional neural network (CNN) [46, 49], which also motivate this work.

In our paper, neural networks are utilized to predict macroscopic parameters (effective permeability, coarse-grid homogenized stiffness matrix, and right-hand side vector). Here, a machine learning method is developed using deep neural network and graphics processing unit (GPU) during the training procedure via two experiments. In particular, we predict an effective permeability in the first experiment and predict a coarse-grid homogenized matrix together with a right-hand side vector in the second experiment, where the predicted homogenized stiffness matrix contains information on how the Richards equation's nonlinearity is tackled, which is a new contribution. For various input random permeability fields, a corresponding set of targets (desired output) is employed to train the neural networks. Fast and accurate computations can be conducted once neural networks have been trained on the training data. Our numerical results show that the deep networks produce favorable results and that they can be applied well to the testing data.

The paper is organized as follows. In Section 2, we begin with Subsection 2.1 about model problem for the underlying Richards equation that characterizes the unsaturated flow within non-periodic heterogeneous media, then Subsection 2.2 regards coarse-scale discretization as well as Picard iteration for linearization, and the numerical homogenization for nonlinear Richards equation is introduced in Subsection 2.3. Next, the concept of employing deep learning as a stand-in for numerical homogenization prediction is described in Section 3, where the sampling is thoroughly discussed, and the networks are carefully defined. In Section 4, we give numerical examples (especially for solutions) to demonstrate the performance of our proposed networks, using predictions of effective permeability and coarse-grid homogenized stiffness matrix along with right-hand side vector, by several cases with various configurations. Section 5 provides a summary and conclusion. Global convergence of Picard linearization process is shown in Appendix A.

2. PRELIMINARIES

2.1. Model problem. In \mathbb{R}^d , let Ω be a computational domain that is open, bounded, convex, Lipschitz, and simply connected. Throughout this work, the case $d = 2$ is investigated to make our discussion clearer, but the concept can be simply extended to $d = 3$ as well. Latin indices (as i, j) are in $\{1, 2\}$. The symbols ∇ and $\frac{\partial}{\partial t}$ respectively indicate

the spatial gradient and temporal derivative, across this paper. Further notation follows [37, 36]. Bold letters (e.g., \mathbf{v} and \mathbf{T}) stand for vector fields and matrix fields over Ω , while italic capitals (e.g., f) are used to represent functions. The spaces of functions, vector fields, and matrix fields over Ω are described by italic capitals (e.g., $L^2(\Omega)$), boldface Roman capitals (e.g., \mathbf{V}), and special Roman capitals (e.g., \mathbb{S}), respectively.

The L^2 inner product is symbolized by (\cdot, \cdot) , and the Sobolev space $V := H_0^1(\Omega) = W_0^{1,2}(\Omega)$ has the norm $\|\cdot\|_V$:

$$\|v\|_V = \left(\|v\|_{L^2(\Omega)}^2 + \|\nabla v\|_{L^2(\Omega)}^2 \right)^{\frac{1}{2}}.$$

Herein, $\|\nabla v\|_{L^2(\Omega)} := \| |\nabla v| \|_{L^2(\Omega)}$, where $|\nabla v|$ specifies the Euclidean norm of the 2-component vector-valued function ∇v . We also let $\mathbf{V} = V^2 = [H_0^1(\Omega)]^2$. For any $\mathbf{v} = (v_1, v_2) \in \mathbf{V}$, it holds that $\|\nabla \mathbf{v}\|_{L^2(\Omega)} := \| |\nabla \mathbf{v}| \|_{L^2(\Omega)}$, having $|\nabla \mathbf{v}|$ as the Frobenius norm of the 2×2 matrix $\nabla \mathbf{v}$.

In the literature, the form of time-dependent Richards equation [40] is usually

$$(2.1) \quad \frac{\partial \Theta(p(t, \mathbf{x}))}{\partial t} - \operatorname{div}(\kappa(\mathbf{x}, p(t, \mathbf{x})) \nabla p(t, \mathbf{x})) = f(t, \mathbf{x}) \text{ in } (0, T] \times \Omega,$$

where $T > 0$ denotes the terminal time. This equation has the initial condition $p(0, \mathbf{x}) = p_0$ in Ω and the Dirichlet boundary condition $p(t, \mathbf{x}) = 0$ on $(0, T] \times \partial\Omega$. The fundamental notation can be found in [36]. Here, volumetric soil water content is denoted by $\Theta(p(t, \mathbf{x}))$, the pressure head is described by $p := p(t, \mathbf{x})$, the unsaturated hydraulic conductivity is represented by $\kappa(p) := \kappa(\mathbf{x}, p)$, and the source or sink function is abbreviated by f .

As in [36], we remark that the volumetric water content $\Theta(p)$ in (2.2) is often a nonlinear function of the pressure head p , and it has the form as follows [4]:

$$\frac{\partial \Theta(p)}{\partial t} = C(p) \frac{\partial p}{\partial t}.$$

The nonlinear hydraulic conductivity $\kappa(\mathbf{x}, p)$ is important for homogenization in this paper. On the other hand, $C(p)$ part is not necessary and can be eliminated, resulting in the identity function $\Theta(p) = p$ in our considering Richards equation:

$$(2.2) \quad \frac{\partial p(t, \mathbf{x})}{\partial t} - \operatorname{div}(\kappa(\mathbf{x}, p(t, \mathbf{x})) \nabla p(t, \mathbf{x})) = f(t, \mathbf{x}) \text{ in } (0, T] \times \Omega.$$

Later, one can see that Eq. (2.2) has a multiscale high-contrast coefficient $\kappa(\mathbf{x}) = \kappa(\mathbf{x}, \omega)$, which is generally stochastic [48]. But for simplicity, the stochasticity notation ω is omitted.

We assume that the hydraulic conductivity and its spatial gradient are uniformly bounded, particularly, there exist positive constants $\underline{\kappa}$ and $\overline{\kappa}$ satisfying the following inequalities:

$$(2.3) \quad \underline{\kappa} \leq \kappa(\mathbf{x}, p), \quad |\nabla \kappa(\mathbf{x}, p)| \leq \overline{\kappa}.$$

Also, it is assumed that the initial condition is

$$(2.4) \quad p_0 = p(0, \mathbf{x}) \in V,$$

without losing generality.

The following bilinear form is defined with a given $u \in V$: for all $p, v \in V$,

$$(2.5) \quad a(p, v; u) = \int_{\Omega} \kappa(u) \nabla p \cdot \nabla v \, dx.$$

Then, (2.2) possesses the variational form as follows: find $p \in V$ such that

$$(2.6) \quad \left(\frac{\partial p}{\partial t}, v \right) + a(p, v; p) = (f, v),$$

with all $v \in V$, for a.e. $t \in (0, T]$, and $f(t, \cdot) \in L^2(\Omega)$. In (2.4), the initial condition was specified.

2.2. Coarse-scale discretization and Picard iteration for linearization. We utilize an efficient Picard iterative technique as described in [31, 42, 14, 33, 32] to deal with the nonlinearity of our problem. For the time-dependent Richards equation, such an iterative algorithm is provided in this section.

To achieve the first purpose of (2.6)'s time discretization (see, for example, [31, 42]), we shall employ the classical backward Euler finite-difference method: find $p \in V$ such that for all $v \in V$,

$$(2.7) \quad \left(\frac{p_{s+1} - p_s}{\tau}, v \right) + a(p_{s+1}, v; p_{s+1}) = (f_{s+1}, v),$$

where we separate the time domain $[0, T]$ uniformly into S intervals, the size of temporal step is $\tau = T/S > 0$, and a function's evaluation at the time $t_s = s\tau$ is designated by the subscript s (for $s = 0, 1, \dots, S$).

The nonlinearity in space will then be tackled by Picard linearization iteration (see, for example, [31, 42, 14]) as follows. Provided p_s , at the time step $(s+1)$ th, $p_{s+1}^0 \in V$ is guessed. With $n = 0, 1, 2, \dots$, find $p_{s+1}^{n+1} \in V$ such that for all $v \in V$,

$$(2.8) \quad \left(\frac{p_{s+1}^{n+1} - p_s}{\tau}, v \right) + a(p_{s+1}^{n+1}, v; p_{s+1}^n) = (f_{s+1}, v).$$

Equivalently,

$$(2.9) \quad \left(\frac{p_{s+1}^{n+1}}{\tau}, v \right) + a(p_{s+1}^{n+1}, v; p_{s+1}^n) = \left(\frac{p_s}{\tau}, v \right) + (f_{s+1}, v).$$

In [38], one can find the proof for existence and uniqueness of solution p_{s+1}^{n+1} to the linearized equation (2.8). As n comes to ∞ , the Picard iterative process converges to a limit, which is theoretically proved in Appendix A. Numerically, this process is finished when it approaches some α th iteration at a specified stopping requirement. To go to the next temporal step in (2.7), the prior time data is set as

$$(2.10) \quad p_{s+1} = p_{s+1}^\alpha$$

All over this paper, we propose a halting indicator based on the relative successive difference, which states that provided a user-defined tolerance $\delta_0 > 0$, if

$$(2.11) \quad \frac{\|p_{s+1}^{n+1} - p_{s+1}^n\|_{L^2(\Omega)}}{\|p_{s+1}^n\|_{L^2(\Omega)}} \leq \delta_0,$$

then the iteration procedure is ended. In Section 4, $\delta_0 = 10^{-6}$ is chosen.

The fine-grid notation is now discussed. In order to solve the local problem (2.13)–(2.14), we let \mathcal{T}_h (*fine grid*) be a conforming triangular partition for the computational domain Ω , having local grid sizes $h_P := \text{diam}(P) \forall P \in \mathcal{T}_h$, and $h := \max_{P \in \mathcal{T}_h} h_P$. The size h is assumed to be small enough so that the fine-grid solution is reasonably near the correct solution. In numerical simulation, the fine grid possesses equal squares, where we employ a fine-scale triangulation whose two triangle components are built inside each square cell, as shown in Fig. 1 below. It is worth noting that the fine grid \mathcal{T}_h is only used to numerically handle local problems.

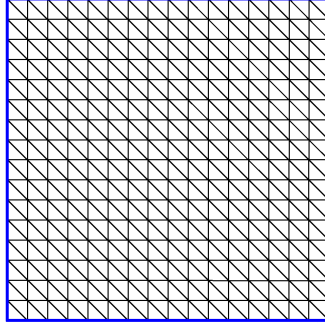


FIGURE 1. Illustration of a triangular fine grid in one coarse block.

Next, we review the coarse grid conception, which will be used to discretize the variational problem (2.6). The first step is dividing Ω into finite elements. This partition is known as coarse grid \mathcal{T}^H , which has \mathcal{T}_h as a refinement. An element K in \mathcal{T}^H is referred to as a coarse-grid block (which is also called coarse-grid cell, coarse element, or coarse patch). Furthermore, the coarse-grid size H is defined as the side length of each square coarse cell, with $H \gg h$. The number of coarse blocks is N_b , while the number of coarse-grid nodes is N_v . Then, $\{\mathbf{x}_k\}_{k=1}^{N_v}$ exhibits the set of all coarse nodes (vertices). A coarse grid is shown in Figure 2.

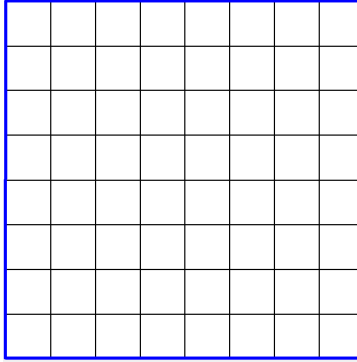


FIGURE 2. Illustration of a coarse grid, where each smallest square is a coarse block.

With regard to the coarse grid \mathcal{T}^H , let V^H be the first-order Galerkin (standard) finite element basis space:

$$V^H := \{v \in V : v|_P \text{ is a polynomial of degree } \leq 1 \ \forall P \in \mathcal{T}^H\}.$$

In this V^H , provided an initial $p_{H,0} = P_H p_0$, where p_0 is from (2.4) and P_H is the $L^2(\Omega)$ projection operator onto V^H .

The fully Picard discrete scheme in \mathcal{T}^H is as follows: We start with an initial $p_{H,0} \in V^H$, and guess $p_{H,s+1}^0 \in V^H$ at the $(s+1)$ th time step, then do iteration in V^H for $p_{H,s+1}^{n+1} \in V^H$:

$$(2.12) \quad \left(\frac{p_{H,s+1}^{n+1} - p_{H,s}}{\tau}, v \right) + a(p_{H,s+1}^n, v; p_{s+1}^n) = (f_{H,s+1}, v),$$

with all $v \in V^H$, and $n = 0, 1, 2, \dots$, until running into (2.11) at some Picard step α th. To advance to the next time step in (2.7), we employ (2.10) to establish the prior time data $p_{H,s+1} = p_{H,s+1}^\alpha$.

2.3. Numerical homogenization. The purpose of this section is to obtain numerical homogenization of the nonlinear Richards equation (2.2) as coarse-grid approximation. We follow the numerical homogenization scheme in [5, 29] (nonlinear) and thanks to [45] (linear). More specifically, the effective coefficient is first numerically calculated. The homogenized Richards equation is then solved on coarse grid as in Subsection 2.2, where the nonlinearity may be treated as a constant at each Picard iteration step (after temporal discretization). We denote the volume average over any $K \in \mathcal{T}^H$ as follows:

$$\langle \cdot \rangle_K = \frac{1}{|K|} \int_K (\cdot) \, dx.$$

2.3.1. Effective coefficient. The effective coefficient $\tilde{\kappa}$ (also known as homogenized coefficient or effective parameter [5]) is computed numerically in this work. We consider the Richards equation (2.2) in non-periodic heterogeneous media. The piecewise constant nonlinear function $\tilde{\kappa}(\mathbf{x}, s)$ in variable \mathbf{x} over \mathcal{T}^H is defined for any $s \in \mathbb{R}$ as follows.

First, let $\psi_j(\mathbf{x})$ ($j = 1, \dots, d$) be the fine-scale solution of the following problem for any $K \in \mathcal{T}^H$ and $s \in \mathbb{R}$:

$$(2.13) \quad -\operatorname{div}(\kappa(\mathbf{x}, s) \nabla \psi_j) = 0 \quad \text{in } K,$$

$$(2.14) \quad \psi_j = x_j \quad \text{on } \partial K,$$

having $\kappa(\mathbf{x}, s)$ as the random heterogeneous coefficient in \mathbf{x} restricted to the local region $K \in \mathcal{T}^H$, with $\mathbf{x} = (x_1, \dots, x_d)$, for $d = 2$. It is worth noting that this local problem is solved on the fine grid \mathcal{T}_h .

Then, with $j = 1, \dots, d$, the constant tensor $\tilde{\kappa}(s)$ is computed on the current K by

$$(2.15) \quad \tilde{\kappa}(s) \langle \nabla \psi_j \rangle_K = \langle \kappa(\mathbf{x}, s) \nabla \psi_j \rangle_K.$$

As a result, for $j, l = 1, \dots, d$, each entry in the constant matrix $\tilde{\kappa}(s)$ on K has the form [45]

$$(2.16) \quad \tilde{\kappa}_{jl}(s) = \frac{1}{|K|} \int_K \kappa(\mathbf{x}, s) \frac{\partial \psi_j}{\partial x_l} \, dx.$$

Using the Divergence Theorem and (2.14), it holds that (2.15) is well-defined:

$$(2.17) \quad \langle \nabla \psi_j \rangle_K = \frac{1}{|K|} \int_K \nabla \psi_j \, dx = \frac{1}{|K|} \int_{\partial K} \psi_j \, \mathbf{n} \, d\sigma = \mathbf{e}_j + \frac{1}{|K|} \int_{\partial K} (\psi_j - x_j) \, \mathbf{n} \, d\sigma = \mathbf{e}_j,$$

where \mathbf{n} represents the piecewise smooth field (on ∂K) of outward pointing unit normal vectors, and \mathbf{e}_j is the unit vector in the j th direction.

The tensor $\tilde{\kappa}(s)$ is bounded, symmetric, positive definite, as shown by (2.14), (2.15) and (2.17) in the following manner [56]. First, let $w_i = \psi_i - x_i$, for $i = 1, \dots, d$. We have

$$\nabla w_i = \nabla \psi_i - \mathbf{e}_i.$$

Second, (2.17) and (2.15) leads to

$$(2.18) \quad \begin{aligned} \mathbf{e}_i \cdot \tilde{\kappa}(s) \mathbf{e}_j &= \mathbf{e}_i \cdot \tilde{\kappa}(s) \langle \nabla \psi_j \rangle_K = \mathbf{e}_i \cdot \langle \kappa(\mathbf{x}, s) \nabla \psi_j \rangle_K \\ &= \langle \mathbf{e}_i \cdot \kappa(\mathbf{x}, s) \nabla \psi_j \rangle_K = \langle (\nabla \psi_i - \nabla w_i) \cdot \kappa(\mathbf{x}, s) \nabla \psi_j \rangle_K. \end{aligned}$$

Next, by (2.14), Divergence Theorem, the production rule and (2.13), it holds that

$$(2.19) \quad \begin{aligned} 0 &= \int_{\partial K} w_i \mathbf{n} \cdot \kappa(\mathbf{x}, s) \nabla \psi_j \, d\sigma \\ &= \int_K \operatorname{div}(w_i \kappa(\mathbf{x}, s) \nabla \psi_j) \, dx \\ &= \int_K w_i \operatorname{div}(\kappa(\mathbf{x}, s) \nabla \psi_j) \, dx + \int_K \nabla w_i \cdot \kappa(\mathbf{x}, s) \nabla \psi_j \, dx \\ &= \int_K \nabla w_i \cdot \kappa(\mathbf{x}, s) \nabla \psi_j \, dx. \end{aligned}$$

Hence, (2.18) becomes

$$(2.20) \quad \mathbf{e}_i \cdot \tilde{\kappa}(s) \mathbf{e}_j = \langle \nabla \psi_i \cdot \kappa(\mathbf{x}, s) \nabla \psi_j \rangle_K,$$

which also offers a different approach to calculate $\tilde{\kappa}$.

To illustrate the effective coefficient calculation, we consider the Haverkamp model [19, 42] possessing the following constitutive relation for the unsaturated hydraulic conductivity κ :

$$(2.21) \quad \kappa(\mathbf{x}, p(\mathbf{x})) = K_s(\mathbf{x}) K_r(p) = \kappa(\mathbf{x}) \frac{1}{1 + |p|}.$$

Here, $\kappa(\mathbf{x})$ denotes the permeability of soils, $K_r(p)$ represents the relative hydraulic conductivity, $K_s(\mathbf{x})$ stands for the saturated hydraulic conductivity (which is mostly different from the permeability $\kappa(\mathbf{x})$, see [41]). All the multiscale heterogeneity is incorporated in $\kappa(\mathbf{x})$ without regard to p , and $\frac{1}{1 + |p|}$ includes all the nonlinearity. With this Haverkamp model (2.21), over each coarse cell $K \in \mathcal{T}^H$, the effective permeability tensor is denoted by $\tilde{\kappa}$ and obtained from (2.15)–(2.16), where

$$(2.22) \quad \tilde{\kappa}(\mathbf{x}, p(\mathbf{x})) = \tilde{\kappa}(\mathbf{x}) \frac{1}{1 + |p|}.$$

In our two-dimensional case, on each coarse cell $K \in \mathcal{T}^H$, the constant effective permeability tensor $\tilde{\kappa}$ from (2.21) is of the following form

$$(2.23) \quad \tilde{\kappa} = \begin{pmatrix} \tilde{\kappa}_{11} & \tilde{\kappa}_{12} \\ \tilde{\kappa}_{12} & \tilde{\kappa}_{22} \end{pmatrix}.$$

2.3.2. Solving the homogenized Richards equation. Finally, referring to the original equation (2.2), we solve the following homogenized Richards equation on coarse grid with the effective coefficient $\tilde{\kappa}$ (2.16):

$$(2.24) \quad \frac{\partial p(t, \mathbf{x})}{\partial t} - \operatorname{div}(\tilde{\kappa}(\mathbf{x}, p(t, \mathbf{x})) \nabla p(t, \mathbf{x})) = f(t, \mathbf{x}) \text{ in } (0, T] \times \Omega,$$

It is clear that this homogenized Richards equation is principally the same as the original one (2.2), with the exception that scalars become symmetric and positive definite tensors.

For numerical simulations, we consider the time-dependent Richards equation (2.2) employing the Haverkamp model (2.21):

$$(2.25) \quad \frac{\partial p(t, \mathbf{x})}{\partial t} - \operatorname{div} \left(\kappa(\mathbf{x}) \frac{1}{1 + |p|} \nabla p(t, \mathbf{x}) \right) = f(t, \mathbf{x}) \text{ in } (0, 1] \times \Omega,$$

where $\mathbf{x} = (x_1, x_2)$, $f(t, \mathbf{x}) = \cos(\pi x_1) \sin(\pi x_2)$, taking the initial condition $p(0, \mathbf{x}) = p_0 = 0$ in Ω and the Dirichlet boundary condition $p(t, \mathbf{x}) = 0$ on $(0, T] \times \partial\Omega$.

After homogenization (addressed in Subsubsection 2.3.1), we solve the homogenized Richards equation derived from (2.25) on coarse grid with the effective permeability $\tilde{\kappa}$ (2.22) as follows:

$$(2.26) \quad \frac{\partial p(t, \mathbf{x})}{\partial t} - \operatorname{div} \left(\tilde{\kappa}(\mathbf{x}) \frac{1}{1 + |p|} \nabla p(t, \mathbf{x}) \right) = f(t, \mathbf{x}) \text{ in } (0, 1] \times \Omega,$$

having the initial condition $p(0, \mathbf{x}) = p_0$ in Ω and the Dirichlet boundary condition $p(t, \mathbf{x}) = 0$ on $(0, T] \times \partial\Omega$.

We denote

$$\tilde{a}(p, v; u) = \int_{\Omega} \tilde{\kappa}(\mathbf{x}, u) \nabla p \cdot \nabla v \, dx,$$

with a given $u \in V$, for any $p, v \in V$, and $\tilde{\kappa}$ is from (2.16) as well as (2.22). Let P_H stand for the $L^2(\Omega)$ projection operator onto V^H , and p_0 comes from (2.4).

The completely Picard discrete iterative scheme for the homogenized Richards equation (2.26) reads in \mathcal{T}^H : starting with an initial $p_{c,0} = P_H p_0$ in V^H , we guess $p_{c,s+1}^0 \in V^H$ at the time step $(s+1)$ th, and carry out iteration in V^H to find $p_{c,s+1}^{n+1} \in V^H$:

$$(2.27) \quad \left(\frac{p_{c,s+1}^{n+1}}{\tau}, v \right) + \tilde{a}(p_{c,s+1}^{n+1}, v; p_{c,s+1}^n) = \left(\frac{p_{c,s}}{\tau}, v \right) + (f_{s+1}, v),$$

for $n = 0, 1, 2, \dots$, until meeting (2.11) at some α th Picard iteration, with all $v \in V^H$. We use (2.10) to set the preceeding time data $p_{c,s+1} = p_{c,s+1}^\alpha$ to shift to the next temporal step in (2.7).

The finite element basis function at node j (that is \mathbf{x}_j) of the coarse grid \mathcal{T}^H is denoted by $\varphi_j \in V^H$. The subscript c can be removed from the following for the sake of simplicity.

At the time step $(s + 1)$ th, the approximate solution $p_{c,s+1}^{n+1}$ is

$$(2.28) \quad p_{c,s+1}^{n+1} \approx \sum_{j=1}^{N_v} p_{c,s+1}^{n+1}(\mathbf{x}_j) \varphi_j = \sum_{j=1}^{N_v} p_{c,s+1,j}^{n+1} \varphi_j,$$

where $p_{c,s+1,j}^{n+1}$ is the nodal point value of $p_{c,s+1}^{n+1}$ at the node j , and N_v is the total number of nodes on the coarse grid \mathcal{T}^H . Let

$$(2.29) \quad \mathbf{p}_{c,s+1}^{n+1} = (p_{c,s+1,1}^{n+1}, p_{c,s+1,2}^{n+1}, \dots, p_{c,s+1,N_v}^{n+1}).$$

Using the above form (2.28) and [4], we can write

$$(2.30) \quad \kappa(\mathbf{x}, p_{c,s+1}^n) \approx \sum_{j=1}^{N_v} \kappa(\mathbf{x}_j, p_{c,s+1,j}^n) \varphi_j = \sum_{j=1}^{N_v} \kappa_j \varphi_j.$$

With N_v defined in (2.28) and for $i, j = \overline{1, N_v}$, we let

$$(2.31) \quad \mathbf{C}_{s+1} = \{C_{s+1,ij}\}, \quad \tilde{\mathbf{A}}_{s+1}^n = \{\tilde{A}_{s+1,ij}^n\}, \quad \mathbf{b}_{s+1} = \{b_{s+1,i}\},$$

where

$$(2.32) \quad \begin{aligned} C_{s+1,ij} &= \int_{\Omega} \varphi_j \cdot \varphi_i \, dx, \\ \tilde{A}_{s+1,ij}^n &= \int_{\Omega} \tilde{\kappa}(\mathbf{x}, p_{c,s+1}^n) \nabla \varphi_j \cdot \nabla \varphi_i \, dx, \\ b_{s+1,i} &= \int_{\Omega} \left(\frac{p_s}{\tau} + f_{s+1} \right) \varphi_i \, dx. \end{aligned}$$

Benefiting from [21], we write (2.27) in the following matrix form:

$$(2.33) \quad \mathbf{C}_{s+1} \frac{\mathbf{p}_{c,s+1}^{n+1}}{\tau} + \tilde{\mathbf{A}}_{s+1}^n \mathbf{p}_{c,s+1}^{n+1} = \mathbf{b}_{s+1},$$

where $\tilde{\mathbf{A}}_{s+1}^n$ denotes the coarse-scale homogenized stiffness matrix, \mathbf{b}_{s+1} represents the right-hand side load vector, each of $\mathbf{p}_{c,s+1}^n$ and $\mathbf{p}_{c,s+1}^{n+1}$ is a vector of N_v components defined in (2.29).

3. DEEP LEARNING FOR NUMERICAL HOMOGENIZATION

Regarding applications of the Richards equation (2.25) as an unsaturated flow, on the one hand, the numerical homogenization gives us a quick solver to calculate the homogenized solutions efficiently and precisely. On the other hand, there exist uncertainties in some local portions of the heterogeneous permeability field $\kappa(\mathbf{x}, p(\mathbf{x}))$. To estimate the flow solution's uncertainties, several thousand forward simulations are required. We want to design a strategy that uses a given vast volume of simulation data and reduces direct calculating endeavor afterwards. For example, convolutional neural network (CNN) has recently been applied to numerical homogenization [46, 49]. In this paper, we assume that the Picard iterative procedure (2.27) for the homogenized Richards equation (2.26) stops at the $(s + 1)$ th time step and $(n + 1)$ th Picard step in (2.27). Then, deep neural networks (DNNs) are utilized to describe the link between stochastic permeability field

$\kappa(\mathbf{x})$ and expected numerical homogenization's macroscopic parameters, that is, coarse-scale effective permeability $\tilde{\kappa}(\kappa)$ (2.23), homogenized stiffness matrix $\tilde{\mathbf{A}}^n(\kappa)$ (2.31) (by data obtained from the n th Picard step) as well as the right-hand side vector $\mathbf{b}(\kappa)$ (2.32) of (2.27). Note that our stochastic permeability fields are generated using Karhunen-Loève expansion (KLE) [48]. Subsequent to the above relation's establishment, for any random permeability field realization, we can feed it to the network and get relevant DNN-prediction of numerical homogenization's macroscopic parameters (to be specified in Subsection 3.1), which will be applied to Subsubsection 2.3.2 for computing the predicted global coarse-scale solution of (2.26). For simplicity in the rest of this work, we will drop the subscript $(s + 1)$ where Picard steps are involved.

More specifically, in order to create the neural network, we are intrigued by building the nonlinear maps g_κ , g_A^n , and g_b that respectively map the permeability field κ to the desired macroscopic parameters (effective permeability $\tilde{\kappa}(\kappa)$, coarse-scale homogenized stiffness matrix $\tilde{\mathbf{A}}^n(\kappa)$, and right-hand side vector $\mathbf{b}(\kappa)$ of (2.27)) as follows:

$$(3.1) \quad g_\kappa : \kappa \rightarrow \tilde{\kappa}(\kappa),$$

$$(3.2) \quad g_A^n : \kappa \rightarrow \tilde{\mathbf{A}}^n(\kappa),$$

$$(3.3) \quad g_b : \kappa \rightarrow \mathbf{b}(\kappa).$$

This study's purpose is to take advantage of deep learning to create rapid approximations of the above expected macroscopic parameters related to the permeability field κ 's uncertainties, allowing us to solve the homogenized Richards equation (2.26) quickly and accurately. For each permeability field κ , its images can be calculated thanks to the maps g_κ , g_A^n , and g_b . We utilize these forward computations as training samples for constructing deep neural networks, which will approximate the associated maps, that is,

$$(3.4) \quad \begin{aligned} \mathcal{N}_\kappa(\kappa) &\approx g_\kappa(\kappa), \\ \mathcal{N}_A^n(\kappa) &\approx g_A^n(\kappa), \\ \mathcal{N}_b(\kappa) &\approx g_b(\kappa). \end{aligned}$$

Within such neural networks, the input is permeability field κ ; whereas the predicted outputs are macroscopic parameters, expressly, effective permeability $\tilde{\kappa}(\kappa)$, coarse-scale homogenized stiffness matrix $\tilde{\mathbf{A}}^n(\kappa)$, and right-hand side vector $\mathbf{b}(\kappa)$ of (2.27). Upon constructing these neural networks, they can be used for any new permeability realization κ , to predict output macroscopic parameters $\tilde{\kappa}_{\text{pred}}$, $\tilde{\mathbf{A}}_{\text{pred}}^n$, and \mathbf{b}_{pred} , which will be defined below.

3.1. Network Architecture. The neurons in most deep neural networks can be arranged into three categories: the input layer, then one or several hidden layers, and finally the output layer. In the majority of deep neural network architectures, these layers are organized in a chain pattern, where each layer acts as a function of the layer before it [39, 17]. Thus, at least one hidden layer exists in every neural network (also called artificial neural network); otherwise, a neural network is not what it is. Deep neural networks are described as having at least two or usually many more hidden layers.

Normally, an L -layer feedforward and fully connected deep neural network \mathcal{N}^L can be represented in the following form [51, 39, 17]:

$$(3.5) \quad \mathcal{N}(z; \theta) = \mathcal{N}^L(z; \theta) = \sigma^L(\mathbf{W}^L \sigma^{L-1}(\dots \sigma^2(\mathbf{W}^2 \sigma^1(\mathbf{W}^1 z + \mathbf{c}^1) + \mathbf{c}^2) \dots) + \mathbf{c}^L),$$

where z is the input layer, L is the network's depth as the number of layers (excluding the input layer), $\theta := (\mathbf{W}^1, \mathbf{W}^2, \dots, \mathbf{W}^L, \mathbf{c}^1, \mathbf{c}^2, \dots, \mathbf{c}^L)$ with the bias vectors \mathbf{c}^l as well as the weight matrices \mathbf{W}^l (for $l = 1, \dots, L$), and σ^l are the activation functions (which are often nonlinear as SELU or ReLU for the input layer or hidden layers).

More specifically, the input layer of this neural network is

$$\mathcal{N}^0(z) = z.$$

For $1 \leq l < L$, the l th hidden layer of the network is

$$\mathcal{N}^l(z) = \sigma^l(\mathbf{W}^l \mathcal{N}^{l-1}(z) + \mathbf{c}^l).$$

The output layer (without using any activation function) is

$$\mathcal{N}^L(z) = \mathbf{W}^L \mathcal{N}^{L-1}(z) + \mathbf{c}^L.$$

A neural network of this type is utilized for approximating the expected output y (also known as target, desired output, correct output, or training value). By solving the following optimization problem, we aim at determining θ^* :

$$(3.6) \quad \theta^* = \underset{\theta}{\operatorname{argmin}} \mathcal{L}(\theta).$$

Here, $\mathcal{L}(\theta)$ stands for the loss function and represents the difference's measurement between the image (predicted output) of the network $\mathcal{N}(z; \theta)$'s input and the target y in a training set consisting of training pairs (z_ν, y_ν) , which are also called training samples, or training examples, or training patterns. In this work, the loss function is the mean squared error:

$$(3.7) \quad \mathcal{L}(\theta) = \frac{1}{N} \sum_{\nu=1}^N \|y_\nu - \mathcal{N}(z_\nu; \theta)\|_2^2,$$

where N represents how many training samples there are. Figure 3 depicts an example of a deep neural network (to be explained below).

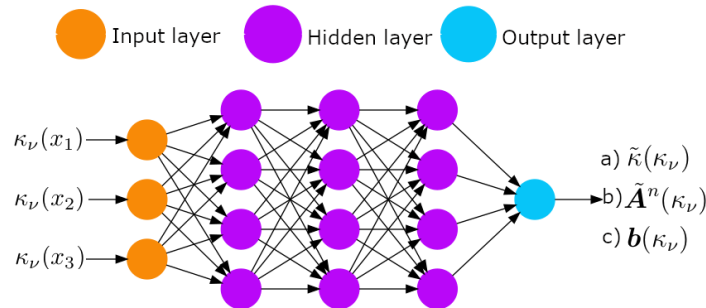


FIGURE 3. Illustration of a deep neural network.

Consider that we are given a collection of distinct permeability realizations $\{\kappa_\nu\}_{\nu=1}^N$ over the whole domain Ω . Within our neural network, the input $z_\nu = \kappa_\nu \in \mathbb{R}^m$ is a vector (named input vector or feature vector) representing the permeability field's values as features $\kappa_\nu(\mathbf{x}_1), \kappa_\nu(\mathbf{x}_2), \dots, \kappa_\nu(\mathbf{x}_m)$, where $\mathbf{x}_1, \mathbf{x}_2, \dots, \mathbf{x}_m \in \mathbb{R}^d$ are the spatial points in the domain Ω , with $m = 256$ and $d = 2$ in our simulations. Recall that our stochastic permeability fields are produced by Karhunen-Loève expansion (KLE) [48], to be explained in Section 4 on numerical experiments. The correct output y_ν is a vector of a vectorized coarse-grid effective permeability tensor $\tilde{\kappa}(\kappa_\nu)$, or homogenized stiffness matrix $\tilde{\mathbf{A}}^n(\kappa_\nu)$, or right-hand side vector $\mathbf{b}(\kappa_\nu)$ of (2.27) by numerical homogenization in Subsection 2.3. The deep neural networks $\mathcal{N}_\kappa(z, \theta_\kappa)$, $\mathcal{N}_A^n(z, \theta_A)$, and $\mathcal{N}_b(z, \theta_b)$ described in (3.4) and (3.5) are trained using the training pairs (z_ν, y_ν) by minimizing the loss function \mathcal{L} with regard to θ as the network parameter, so that the trained neural networks $\mathcal{N}_\kappa(z, \theta_\kappa^*)$, $\mathcal{N}_A^n(z, \theta_A^*)$, and $\mathcal{N}_b(z, \theta_b^*)$ can respectively estimate the functions g_κ , g_A^n , and g_b in (3.1)–(3.3) on coarse grid. After creating the neural networks, we utilize them for any new permeability field $\kappa_{N+\iota}$ ($\iota = 1, \dots, M$) to quickly predict the coarse-scale outputs, which are effective permeability $\tilde{\kappa}_{\text{pred}}$ by

$$(3.8) \quad \tilde{\kappa}_{\text{pred}}(\kappa_{N+\iota}) = \mathcal{N}_\kappa(\kappa_{N+\iota}; \theta_\kappa^*) \approx g_\kappa(\kappa_{N+\iota}) = \tilde{\kappa}(\kappa_{N+\iota}),$$

and homogenized stiffness matrix $\tilde{\mathbf{A}}_{\text{pred}}^n$ by

$$(3.9) \quad \tilde{\mathbf{A}}_{\text{pred}}^n(\kappa_{N+\iota}) = \mathcal{N}_A^n(\kappa_{N+\iota}; \theta_A^*) \approx g_A^n(\kappa_{N+\iota}) = \tilde{\mathbf{A}}^n(\kappa_{N+\iota}),$$

and right-hand side vector \mathbf{b}_{pred} of (2.27) by

$$(3.10) \quad \mathbf{b}_{\text{pred}}(\kappa_{N+\iota}) = \mathcal{N}_b(\kappa_{N+\iota}; \theta_b^*) \approx g_b(\kappa_{N+\iota}) = \mathbf{b}(\kappa_{N+\iota}).$$

3.2. Network-based numerical homogenization solver. Significantly, upon designing the neural networks, following the matrix form (2.33), at the final $(s+1)$ th temporal step and $(n+1)$ th Picard step in (2.27), we can find the predicted global coarse-scale solution $p_{c,\text{pred}}^{n+1}$ of the homogenized Richards equation (2.26) by solving for the coarse-scale coefficient vector $\mathbf{p}_{c,\text{pred}}^{n+1}$ (2.29) from the linear algebraic system

$$(3.11) \quad \mathbf{C}_{s+1} \frac{\mathbf{p}_{c,\text{pred}}^{n+1}}{\tau} + \tilde{\mathbf{A}}_{\text{pred}}^n \mathbf{p}_{c,\text{pred}}^{n+1} = \mathbf{b}_{\text{pred}}.$$

Here, $\tilde{\kappa}_{\text{pred}}$, $\tilde{\mathbf{A}}_{\text{pred}}^n$, and \mathbf{b}_{pred} were predicted in (3.8), (3.9), and (3.10), respectively.

4. NUMERICAL EXAMPLES

Within this part, utilizing our developed deep learning strategy, several numerical results are shown for the predicted macroscopic parameters and thus solutions of the Richards equation's numerical homogenization. More specifically, we investigate the accuracy of deep neural networks (DNNs). Numerical experiments are carried out for the steady-state and time-dependent homogenized Richards equation (2.26) derived from the Haverkamp model (2.25) based on the original Richards equation (2.2). The considered permeability fields $\kappa(\mathbf{x})$ in (2.25) are heterogeneous, high-contrast, and stochastic (to be specified in Subsection 4.1). Some examples of our generated permeabilities are presented in Figure 4. On coarse grid, for each permeability field $\kappa(\mathbf{x})$, we investigate two DNN

approaches: (1) prediction of effective permeability tensor and (2) prediction of homogenized stiffness matrix (for steady-state case) together with prediction of right-hand side vector of (2.27) (for time-dependent case).

In simulations, our computational domain $\Omega = [0, 1] \times [0, 1]$ is heterogeneous and includes uncertainties. We use 8×8 square coarse grid as Fig. 2 (of edge size $H = 1/8$) and its refinement fine grid as Fig. 1 of 128×128 squares with two triangles (of size $h = \sqrt{2}/128$) per square fine cell. The starting guess for pressure of the Picard iteration process is 0. Over all numerical experiments, the Picard iterative termination criterion is $\delta_0 = 10^{-6}$, which ensures this linearization procedure's convergence, and we assume that the final Picard step is $(n + 1)$ th. The maximum number of Picard iterations is 4, for either the steady-state or time-dependent case.

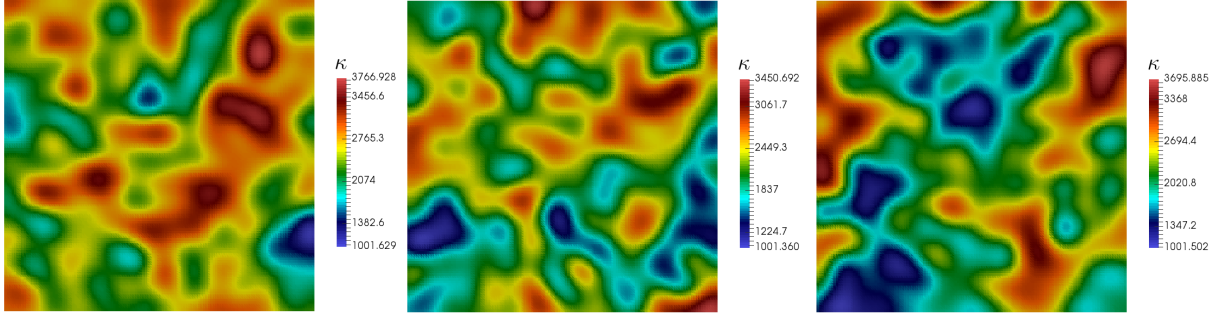


FIGURE 4. Examples of three permeability fields κ in range $[1000, 4200]$.

4.1. Stochastic permeability. In order to parameterize the permeability fields' uncertainties, we employ the Karhunen-Loève expansion (KLE) [1, 48, 49, 15, 55]. Let $\Upsilon(\mathbf{x}, \omega)$ be a random process. Its covariance function is denoted by $R(\mathbf{x}, \hat{\mathbf{x}})$, with the position vectors $\mathbf{x} = (x_1, x_2)$, $\hat{\mathbf{x}} = (\hat{x}_1, \hat{x}_2)$ in Ω . We choose a special orthonormal basis $\{\phi_k(\mathbf{x})\}$ in the Hilbert space $L^2(\Omega)$ such that $\phi_k(\mathbf{x})$ are the eigenfunctions of $R(\mathbf{x}, \hat{\mathbf{x}})$ in the spectral problem

$$(4.1) \quad \int_{\Omega} R(\mathbf{x}, \hat{\mathbf{x}}) \phi_k(\hat{\mathbf{x}}) d\hat{\mathbf{x}} = \lambda_k \phi_k(\mathbf{x}), \quad k = 1, 2, \dots,$$

where λ_k are the eigenvalues. With these ϕ_k and λ_k obtained from (4.1), $\Upsilon(\mathbf{x}, \omega)$ can be expressed in the following form called Karhunen-Loève expansion [55]:

$$(4.2) \quad \Upsilon(\mathbf{x}, \omega) = \sum_{k=1}^{\infty} \sqrt{\lambda_k} \zeta_k(\omega) \phi_k(\mathbf{x}),$$

where $\zeta_k(\omega)$ are the random variables to be found.

In experiments, regarding (4.2), only N_{Υ} leading terms (determined by λ_k 's size) need to be kept to preserve most of $\Upsilon(\mathbf{x}, \omega)$'s energy, and thus,

$$\Upsilon(\mathbf{x}, \omega) = \sum_{k=1}^{N_{\Upsilon}} \sqrt{\lambda_k} \zeta_k(\omega) \phi_k(\mathbf{x}).$$

About the covariance function $R(\mathbf{x}, \hat{\mathbf{x}})$, it is supposed to be of the form

$$(4.3) \quad R(\mathbf{x}, \hat{\mathbf{x}}) = \sigma^2 \exp \left(- \sqrt{\frac{|x_1 - \hat{x}_1|^2}{\eta_1^2} + \frac{|x_2 - \hat{x}_2|^2}{\eta_2^2}} \right),$$

abbreviated by $\kappa(\mathbf{x})$, where $\eta_1 = 0.2, \eta_2 = 0.2$ are correlation lengths in each spatial direction, and $\sigma^2 = 2$ is the variance. Then, each of our stochastic permeability fields $\kappa(\mathbf{x}, \omega)$ can be represented by

$$(4.4) \quad \kappa(\mathbf{x}, \omega) = \exp(a_k(m(\mathbf{x}, \omega))),$$

where $m(\mathbf{x}, \omega) = m(\Upsilon(\mathbf{x}, \omega))$ is the heterogeneous porosity, and $a_k > 0$. Recall that some examples of our generated permeabilities are presented in Figure 4.

Alternative ways to build a stochastic permeability field can be employed without affecting our described deep learning methodology. The reason is that a separate neural network is created for each of the macroscopic parameters (effective permeability tensor, homogenized stiffness matrix, and right-hand side vector of (2.27)) as follows.

4.2. Overview of deep learning for numerical homogenization. We use the numerical homogenization technique described in Subsection 2.3 to produce the coarse-scale sample pairs (by data obtained from the n th Picard step of (2.27)). The stochastic permeability field $z = \kappa$ is viewed as the neural network's input, whereas the desired outputs are coarse-scale effective permeability tensor $\tilde{\kappa}$ (2.23), homogenized stiffness matrix $\tilde{\mathbf{A}}^n$ (2.31) (for steady-state case) along with right-hand side vector \mathbf{b} (2.32) from (2.27) (for time-dependent case). We arbitrarily split up these sample pairs into the training set (also known as training data, training dataset, or learning set) and testing set. The training set is formed by sample pairs produced by a high number N of random permeability realizations $\kappa_1, \kappa_2, \dots, \kappa_N$. On the other hand, the testing set consists of the sample pairs constructed by the remaining M random permeability realizations $\kappa_{N+1}, \kappa_{N+2}, \dots, \kappa_{N+M}$, for assessing the trained networks's predictive ability. We note that, in order to create a unique deep neural network, an optimization problem is addressed for each of the macroscopic parameters ($\tilde{\kappa}$, $\tilde{\mathbf{A}}^n$, and \mathbf{b}) by minimizing the loss function established by the training set. The network architectures used to train such macroscopic parameters are summarized as follows (with $m = 256 = 16 \times 16$ and $\mathbf{x}_1, \mathbf{x}_2, \dots, \mathbf{x}_m \in \mathbb{R}^2$):

- a) For the effective permeability $\tilde{\kappa}$, we generate a network \mathcal{N}_κ using
 - Input: vectorized permeability field κ_ν of values $\kappa_\nu(\mathbf{x}_1), \kappa_\nu(\mathbf{x}_2), \dots, \kappa_\nu(\mathbf{x}_m)$,
 - Desired output: vectorized effective permeability $\tilde{\kappa}(\kappa_\nu)$ of 256 entries,
 - Loss function (3.7): mean squared error $\frac{1}{N} \sum_{\nu=1}^N \|\tilde{\kappa}(\kappa_\nu) - \mathcal{N}_\kappa(\kappa_\nu; \theta_\kappa)\|_{\mathbb{L}^2(\Omega)}^2$,
 - Activation function: SELU (Scaled Exponential Linear Unit) activation function for the first input layer, then ReLU (Rectified Linear Unit) activation function for all hidden layers, no activation function at the last output layer,
 - DNN structure: 3 hidden layers, each layer comprises 128-356 neurons,
 - Kernel initializer: normal,
 - Training optimizer: Adam.

- b) For the coarse-grid homogenized stiffness matrix $\tilde{\mathbf{A}}^n$, we create a network \mathcal{N}_A^n employing
- Input: vectorized permeability field κ_ν of values $\kappa_\nu(\mathbf{x}_1), \kappa_\nu(\mathbf{x}_2), \dots, \kappa_\nu(\mathbf{x}_m)$,
 - Desired output: vectorized coarse-scale homogenized stiffness matrix $\tilde{\mathbf{A}}^n(\kappa_\nu)$ of 375 entries,
 - Loss function (3.7): mean squared error $\frac{1}{N} \sum_{\nu=1}^N \|\tilde{\mathbf{A}}^n(\kappa_\nu) - \mathcal{N}_A^n(\kappa_\nu; \theta_A)\|_{\mathbb{L}^2(\Omega)}^2$,
 - Activation function: SELU activation function for the first input layer, then ReLU activation function for all hidden layers, no activation function at the last output layer,
 - DNN structure: 3 hidden layers, each layer consists of 384-512 neurons,
 - Kernel initializer: normal,
 - Training optimizer: Adam.
- c) For the right-hand side vector \mathbf{b} of (2.27), we generate a network \mathcal{N}_M^n having
- Input: vectorized permeability field κ_ν of values $\kappa_\nu(\mathbf{x}_1), \kappa_\nu(\mathbf{x}_2), \dots, \kappa_\nu(\mathbf{x}_m)$,
 - Desired output: right-hand side vector $\mathbf{b}(\kappa_\nu)$ of (2.27) with 81 entries,
 - Loss function (3.7): mean squared error $\frac{1}{N} \sum_{\nu=1}^N \|\mathbf{b}(\kappa_\nu) - \mathcal{N}_M^n(\kappa_\nu; \theta_b)\|_{\mathbb{L}^2(\Omega)}^2$,
 - Activation function: SELU activation function for the first input layer, then ReLU activation function for all hidden layers, no activation function for the last output layer,
 - DNN structure: 3 hidden layers, each layer contains 256-384 neurons,
 - Kernel initializer: normal,
 - Training optimizer: Adam.

We utilize the activation functions SELU (Scaled Exponential Linear Unit) [26] and ReLU (Rectified Linear Unit) [16] because of their proved enablement in training deep neural networks without any vanishing gradient problem. Moreover, ReLU has the simplest derivative out of all nonlinear activation functions. SELU is less common than ReLU, but SELU is very promising thanks to the fact that as opposed to ReLU, SELU cannot die. By definition, SELU induces self-normalization neural network (SNN), and neuronal activations in the SNN automatically reach a zero mean and unit standard deviation. SELU alone learns more quickly and effectively than other activation functions. The optimizer Adam (Adaptive Moment Estimation) is a further extension of stochastic gradient descent (SGD) and is widely employed in neural network training [25]. Over all experiments, we use Python API Tensorflow and Keras [7] to train our neural network.

Upon training, a neural network is constructed, and we can apply it to output's predicting provided a new input. For the network to be helpful, the predictions must be accurate. Through all experiments, to study the predictive ability of our established network, we employ M sample pairs, which were not touched in the network training. With respect to these sample pairs as the testing set, we compare the predicted output with the target (correct output) and calculate their difference using some appropriate metric (to assess how well the model is working [7]).

Regarding error formulas, over the training dataset on coarse grid, the error computation benefits from the relative l^2 error, namely, root mean square error (RMSE) [47, 54, 57, 22]:

$$(4.5) \quad RMSE = \sqrt{\frac{\sum_{\nu=1}^N |\hat{y}_\nu - y_\nu|^2}{\sum_{\nu=1}^N |y_\nu|^2}},$$

where N is the number of training pairs, y_ν is the target, and \hat{y}_ν is the predicted value for the sample pair (z_ν, y_ν) defined right before (3.7).

On M testing samples, the relative l^2 errors between the targets $(\tilde{\kappa}, \tilde{\mathbf{A}}^n, \mathbf{b})$ and their corresponding predicted coarse-scale effective permeability $\tilde{\kappa}_{\text{pred}}$ (3.8), homogenized stiffness matrix $\tilde{\mathbf{A}}_{\text{pred}}^n$ (3.9), and right-hand side vector \mathbf{b}_{pred} (3.10) of (2.27) are respectively

$$(4.6) \quad \begin{aligned} e_{l^2}^{\tilde{\kappa}}(\kappa_{N+\iota}) &= \frac{|\tilde{\kappa}_{\text{pred}}(\kappa_{N+\iota}) - \tilde{\kappa}(\kappa_{N+\iota})|}{|\tilde{\kappa}(\kappa_{N+\iota})|}, \\ e_{l^2}^{\tilde{\mathbf{A}}}(\kappa_{N+\iota}) &= \frac{|\tilde{\mathbf{A}}_{\text{pred}}^n(\kappa_{N+\iota}) - \tilde{\mathbf{A}}^n(\kappa_{N+\iota})|}{|\tilde{\mathbf{A}}^n(\kappa_{N+\iota})|}, \\ e_{l^2}^{\mathbf{b}}(\kappa_{N+\iota}) &= \frac{|\mathbf{b}_{\text{pred}}(\kappa_{N+\iota}) - \mathbf{b}(\kappa_{N+\iota})|}{|\mathbf{b}(\kappa_{N+\iota})|}, \end{aligned}$$

where $\iota = 1, \dots, M$. Here, the norms were defined in Subsection 2.1, the first two formulas has the Frobenius norm (or entrywise 2-norm) of matrix, and the last formula possesses the Euclidean norm (or 2-norm) of vector. The formulas in (4.6) are also called metrics.

More importantly, to evaluate the accuracy of our proposed DNN approaches for solutions, we employ the following relative L^2 and H^1 (energy) errors:

$$(4.7) \quad \begin{aligned} e_{L^2}^E &= \frac{\|p_{c,\text{pred}}^E(\kappa_{N+\iota}) - p_c(\kappa_{N+\iota})\|_{L^2(\Omega)}}{\|p_c(\kappa_{N+\iota})\|_{L^2(\Omega)}}, & e_{H^1}^E &= \frac{\|\nabla p_{c,\text{pred}}^E(\kappa_{N+\iota}) - \nabla p_c(\kappa_{N+\iota})\|_{L^2(\Omega)}}{\|\nabla p_c(\kappa_{N+\iota})\|_{L^2(\Omega)}}, \\ e_{L^2}^A &= \frac{\|p_{c,\text{pred}}^A(\kappa_{N+\iota}) - p_c(\kappa_{N+\iota})\|_{L^2(\Omega)}}{\|p_c(\kappa_{N+\iota})\|_{L^2(\Omega)}}, & e_{H^1}^A &= \frac{\|\nabla p_{c,\text{pred}}^A(\kappa_{N+\iota}) - \nabla p_c(\kappa_{N+\iota})\|_{L^2(\Omega)}}{\|\nabla p_c(\kappa_{N+\iota})\|_{L^2(\Omega)}}. \end{aligned}$$

In these expressions, p_c is the homogenized solution of (2.33), $p_{c,\text{pred}}^E$ is the solution for (3.11) obtained by DNN-prediction of effective permeability, $p_{c,\text{pred}}^A$ is the solution to (3.11) derived by DNN-prediction of homogenized stiffness matrix (for the steady-state problem) or homogenized stiffness matrix together with right-hand side vector of (2.27) (for the time-dependent problem). All these solutions are achieved from the last Picard step $(n+1)$ th (and at the last time step $(s+1)$ th in the time-dependent case), where the starting guess is 0 for the pressure of Picard iterative procedure.

In experiments, we generate 6000 realizations of random heterogeneous permeability fields. Recall that some samples of permeability fields are presented in Figure 4. These 6000 permeability realizations are then employed to produce 6000 sample pairs. As a typical practice, among these 6000 sample pairs, we arbitrarily pick $N = 5000$ sample pairs as training samples (where 20% of them are for validation) and use the rest $M = 1000$ sample pairs as testing samples.

We should point out that raw data are not often fed directly to neural networks nor statistical models. Usually, data need to be prepared in order to ease the network optimization procedure and increase the chances of getting favorable results. In particular, before training a neural network model, data processing like standardization or normalization are used to rescale input and output variables. When a dataset is standardized, the value distribution is scaled to have a mean of 0 and a standard deviation of 1. Whereas, normalization is the procedure of forcing data to fit within a given range, which is $[-1, 1]$ or $[0, 1]$, and is generally determined by the activation function being used.

In this paper, only data normalization is considered. Specifically, we are interested in a fairly simple normalizing technique, called reciprocal normalization, which normalizes numbers to the range -1 to 1, having the respective normalization and denormalization formulas

$$(4.8) \quad x' = 2 \frac{x - \min}{\max - \min} - 1, \quad x = \left[\frac{x' + 1}{2} (\max - \min) \right] + \min,$$

Here, x' is the normalized value, x is the original (or denormalized) value, \min and \max are respectively the minimum and maximum observable values of the given data. Note that such normalization method is applied to all input and target variables in this study. In simulations, our dataset's normalizing procedure benefits from the scikit-learn object `MinMaxScaler`.

4.3. Experiment for steady-state Richards equation. We first consider in this section the steady-state Richards equation derived from (2.25) as a special case of (2.2): find $p \in V$ such that

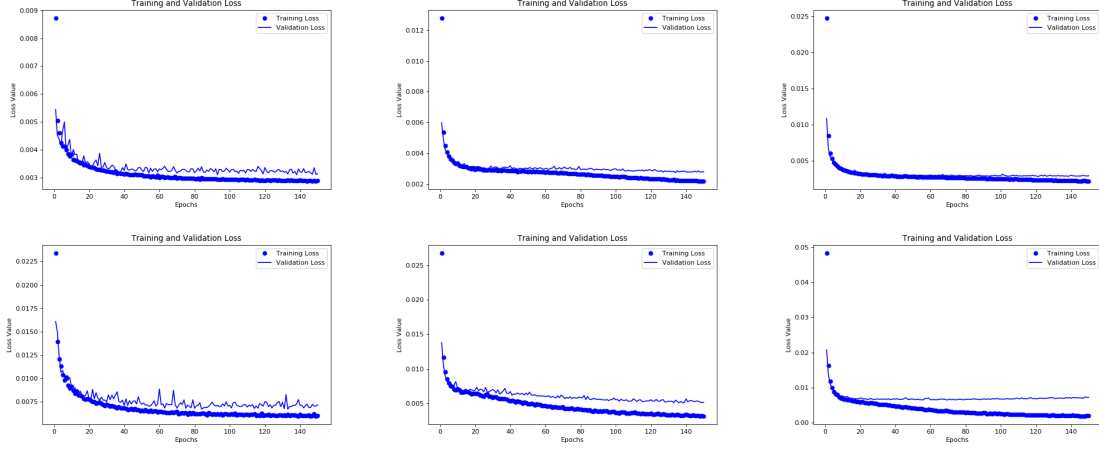
$$(4.9) \quad -\operatorname{div} \left(\kappa(\mathbf{x}) \frac{1}{1 + |p|} \nabla p \right) = f \text{ in } \Omega,$$

with the Dirichlet boundary condition $p(\mathbf{x}) = 0$ on $\partial\Omega$ and $f = 1$.

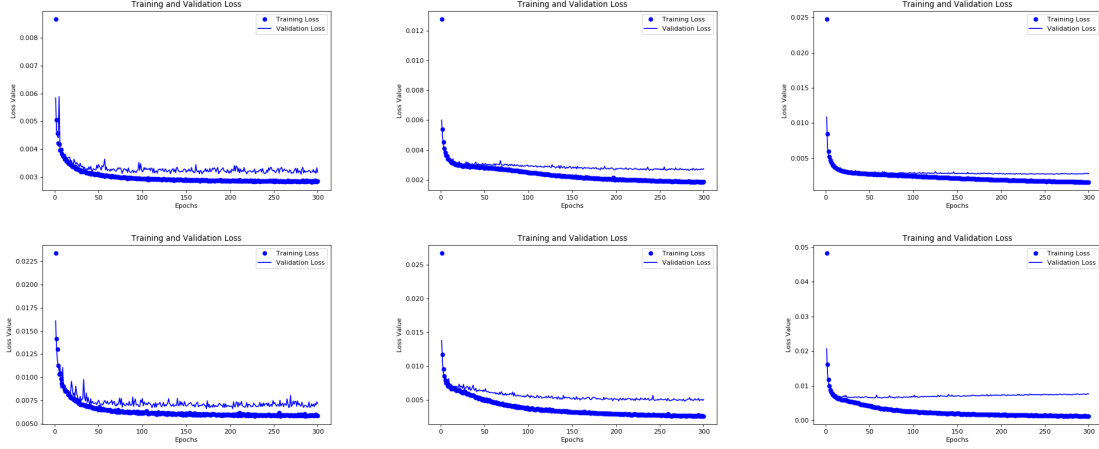
Providing the steady-state form of the homogenized equation (2.26), we compute the macroscopic parameters (effective permeability tensor $\tilde{\kappa}$ (2.23) as well as coarse-scale homogenized stiffness matrix $\tilde{\mathbf{A}}^n$ (2.31)) as in Subsection 2.3 and generate a data set of 6000 samples. Then, 5000 training samples in such dataset are used to build deep neural networks (DNNs) for estimating those macroscopic parameters. To show the convergence of loss function for the neural networks, Fig. 5 plots the relative l^2 error RMSE (4.5) between the DNN-predictions and targets ($\tilde{\kappa}$ and $\tilde{\mathbf{A}}^n$) in the training set (including the validation set) corresponding to epoch number and batch size.

Next, with the established deep neural networks, given 1000 testing pairs, we carry out the testing process for each macroscopic parameter. The minimum, maximum, mean, and one sample relative l^2 errors (4.6) between the DNN-predictions ($\tilde{\kappa}_{\text{pred}}$, $\tilde{\mathbf{A}}_{\text{pred}}^n$) and targets ($\tilde{\kappa}$, $\tilde{\mathbf{A}}^n$) are computed and recorded in Tables 1–3. As one can see from these tables, the predictions' accuracy improves as the number of epochs gets larger. We also take into account the increasing batch size, which leads to the growing learning rate as expected. With regard to accuracy, a very good neural network architecture is employed.

Epochs – 150 / Batch size – 4 Epochs – 150 / Batch size – 16 Epochs – 150 / Batch size – 64



Epochs – 300 / Batch size – 4 Epochs – 300 / Batch size – 16 Epochs – 300 / Batch size – 64



Epochs – 600 / Batch size – 4 Epochs – 600 / Batch size – 16 Epochs – 600 / Batch size – 64

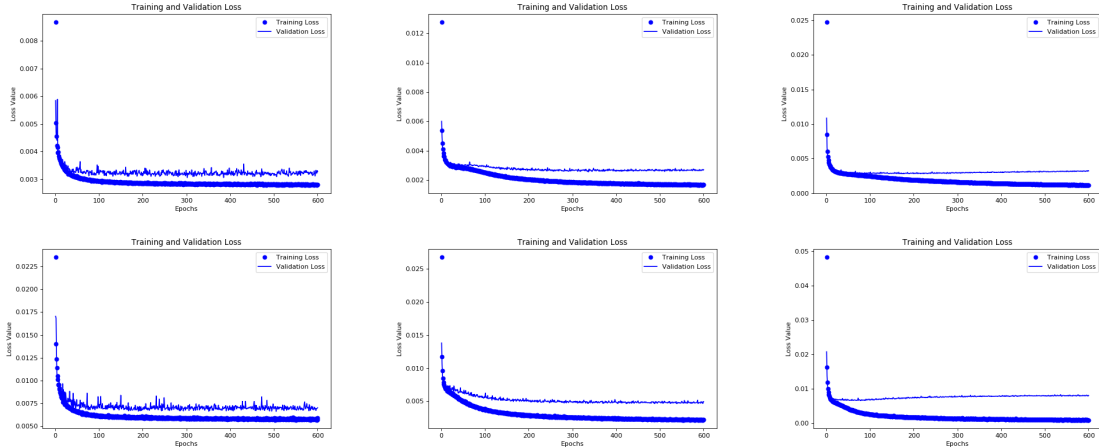


FIGURE 5. Steady-state case (4.9). Prediction's relative l^2 errors RMSE (4.5) over 5000 training samples. First row: for effective permeability. Second row: for homogenized stiffness matrix.

Batch sizes	min	max	mean	one sample	Batch sizes	min	max	mean	one sample
4	2.75	9.53	4.65	4.04	4	1.5	13.24	2.88	1.82
8	2.96	8.47	4.63	4.19	8	1.21	9.44	2.43	1.37
16	2.25	10.16	3.87	2.53	16	1.16	11.17	2.24	1.86
32	2.03	6.96	3.14	2.21	32	0.98	7.42	2.18	1.32
64	2.17	5.96	3.06	2.72	64	1.01	6.64	2.06	1.48

(A) $e_{l^2}^{\tilde{\kappa}}$ (%).

(B) $e_{l^2}^{\tilde{A}}$ (%).

TABLE 1. Steady-state case (4.9). Prediction's relative l^2 errors (4.6) for 150 epochs with different batch sizes on 1000 testing samples: (A) for effective permeability (which is the same as time-dependent cases); (B) for homogenized stiffness matrix (at the final Picard step).

Batch sizes	min	max	mean	one sample	Batch sizes	min	max	mean	one sample
4	2.95	10.08	4.63	3.91	4	1.45	12.62	2.53	2.12
8	3.03	9.86	4.98	4.47	8	1.24	7.63	2.31	1.51
16	2.43	10.61	4.06	3.26	16	1.26	11.61	2.35	1.26
32	2.37	7.85	3.71	2.79	32	1.15	6.05	2.06	1.27
64	1.89	7.93	3.09	2.21	64	0.85	8.66	1.96	1.06

(A) $e_{l^2}^{\tilde{\kappa}}$ (%).

(B) $e_{l^2}^{\tilde{A}}$ (%).

TABLE 2. Steady-state case (4.9). Prediction's relative l^2 errors (4.6) for 300 epochs with different batch sizes on 1000 testing samples: (A) for effective permeability (which is the same as time-dependent cases); (B) for homogenized stiffness matrix (at the final Picard step).

Batch sizes	min	max	mean	one sample	Batch sizes	min	max	mean	one sample
4	3.64	9.31	5.1	4.13	4	0.88	8.66	1.96	2.44
8	3.03	9.06	4.5	3.34	8	1.25	11.95	2.19	1.56
16	2.69	9.95	4.21	3.31	16	1.06	8.95	2.22	1.58
32	2.11	8.39	3.52	3.03	32	1.03	9.23	2.08	1.39
64	1.71	8.42	3.13	2.96	64	0.78	9.71	1.95	1.46

(A) $e_{l^2}^{\tilde{\kappa}}$ (%).

(B) $e_{l^2}^{\tilde{A}}$ (%).

TABLE 3. Steady-state case (4.9). Prediction's relative l^2 errors (4.6) for 600 epochs with different batch sizes on 1000 testing samples: (A) for effective permeability (which is the same as time-dependent cases); (B) for homogenized stiffness matrix (at the final Picard step).

Now, we present numerical results for solution to the homogenized equation of the steady-state problem (4.9), using the first permeability field from Fig. 4. More specifically, Fig. 6 depicts the solution p_c of (2.33) obtained by numerical homogenization, solution $p_{c,\text{pred}}^E$ to (3.11) gained from DNN-prediction of effective permeability, and solution $p_{c,\text{pred}}^A$ from (3.11) attained by DNN-prediction of homogenized stiffness matrix.

Next, numerical experiments are completed on 1000 testing samples. That is, we compare the predicted solution with the homogenized solution p_c (2.33) in relative L^2 and H^1 errors (4.7). In particular, the comparisons between $p_{c,\text{pred}}^E$ (3.11) and p_c (2.33) are presented in Table 4, while the comparisons between $p_{c,\text{pred}}^A$ (3.11) and p_c (2.33) are shown in Table 5. In these tables, we depict mean, minimum, and maximum errors (over 1000 testing samples) as well as one sample errors (using the first permeability field in Fig. 4). It is observable from such results for solutions that DNN-prediction by effective permeability is a little bit more accurate than DNN-prediction by matrix. All predictions have good accuracy, and maximum errors are less than 10%. The difference between mean errors and minimum errors are smaller than the difference between mean errors and maximum errors. This fact indicates that most of the numerical results (by accuracy) are closer to the minimum error. In summary, the DNN-prediction for steady-state Richards equation provides highly accurate solutions.

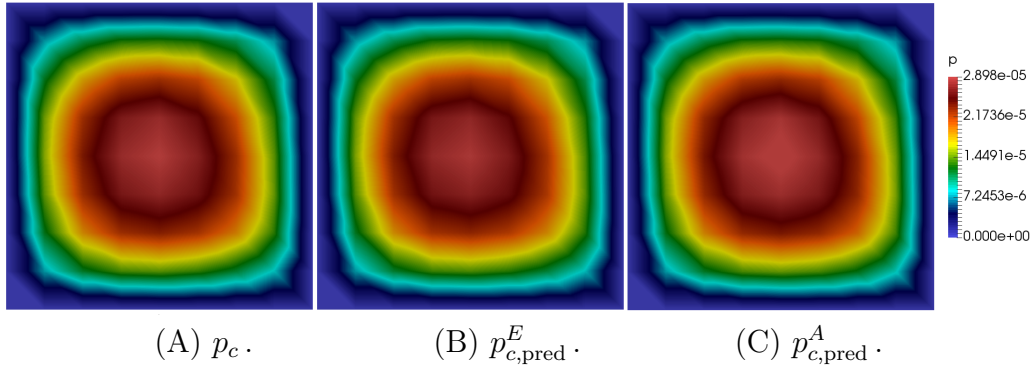


FIGURE 6. Steady-state problem (4.9). Numerical results for solutions (using the first permeability field from Fig. 4): (A) homogenized solution; (B) solution obtained by prediction of effective permeability only; (C) solution obtained by prediction of homogenized stiffness matrix alone.

	$e_{L^2}^E$ (%)	$e_{H^1}^E$ (%)
Mean error	0.967	1.912
Minimum error	0.305	0.843
Maximum error	5.703	6.527
One sample	0.541	1.223

TABLE 4. Steady-state case (4.9). Numerical results for solutions (the case one sample uses the first permeability field from Fig. 4): errors (4.7) between homogenized solution and solution by predicted effective permeability.

	$e_{L^2}^A$ (%)	$e_{H^1}^A$ (%)
Mean error	1.238	2.431
Minimum error	0.321	1.059
Maximum error	5.676	8.034
One sample	0.676	1.778

TABLE 5. Steady-state case (4.9). Numerical results for solutions (the case one sample uses the first permeability field from Fig. 4): errors (4.7) between homogenized solution and solution by DNN-prediction of homogenized stiffness matrix.

4.4. Experiment for time-dependent Richards equation. We investigate in this subsection the time-dependent Richards equation (2.25) as a special case of (2.2): find $p \in V$ such that

$$(4.10) \quad \frac{\partial p(t, \mathbf{x})}{\partial t} - \operatorname{div} \left(\kappa(\mathbf{x}) \frac{1}{1 + |p|} \nabla p(t, \mathbf{x}) \right) = f(t, \mathbf{x}) \text{ in } (0, 1] \times \Omega,$$

where $f(t, \mathbf{x}) = \cos(\pi x_1) \sin(\pi x_2)$, with the initial condition $p(0, \mathbf{x}) = p_0 = 0$ over Ω , and in the company of the Dirichlet boundary condition $p(t, \mathbf{x}) = 0$ on $(0, T] \times \partial\Omega$. We set the terminal time $T = 5 \cdot 10^{-5} = S\tau$ and $S = 20$ time steps, possessing the temporal step size $\tau = T/S = 25 \cdot 10^{-7}$.

Regarding the homogenized equation (2.26) or (2.33), we calculate the macroscopic parameters (effective permeability tensor $\tilde{\kappa}$ (2.23), homogenized stiffness matrix $\tilde{\mathbf{A}}^n$ (2.31) (by data obtained from the n th Picard step), and right-hand side vector \mathbf{b} (2.32) from (2.27)) as in Subsection 2.3 and make 6000 samples. Using 5000 training samples, deep neural networks (DNNs) are created to approximate such macroscopic parameters.

Then, with the constructed deep neural networks, their performance is checked on 1000 testing samples for each of the macroscopic parameters (effective permeability tensor, homogenized stiffness matrix, and right-hand side vector of (2.27)). Note that the coarse-scale homogenized stiffness matrix $\tilde{\mathbf{A}}_{\text{pred}}^n$ (3.9) and right-hand side vector \mathbf{b}_{pred} (3.10) of (2.27) are predicted for the last temporal step $(s + 1)$ th and at the last Picard iteration step $(n + 1)$ th, by data obtained from the n th Picard step. Whereas, we predict the effective permeability field $\tilde{\kappa}_{\text{pred}}$ (3.8) only once in Subsection 4.3 within Tables 1–3a, as there is not any time change. Tables 6–8 show the relative l^2 errors (4.6) between the targets $(\tilde{\mathbf{A}}^n, \mathbf{b})$ and predictions $(\tilde{\mathbf{A}}_{\text{pred}}^n, \mathbf{b}_{\text{pred}})$, at the last temporal step and final Picard step. These Tables 6–8 demonstrate that the best results are obtained with 300 epochs and batch size 64, which will be used for prediction in the rest of this paper.

For this time-dependent problem (2.25), the DNN-prediction by matrix and vector is also operated on 5 time steps (1st, 5th, 10th, 15th, 20th). Over these temporal steps, Fig. 7 presents the relative l^2 errors (4.6) between the targets $(\tilde{\mathbf{A}}^n, \mathbf{b})$ and predictions $(\tilde{\mathbf{A}}_{\text{pred}}^n, \mathbf{b}_{\text{pred}})$ over 1000 testing samples. That errors are fairly small, and the largest errors are less than 8%.

Batch sizes	min	max	mean	one sample
4	1.23	10.88	2.25	1.14
8	1.00	10.25	1.95	1.36
16	0.95	6.91	1.87	1.39
32	0.81	7.31	1.89	1.41
64	0.88	6.02	1.68	1.27

(A) $e_{l^2}^A$ (%).

Batch sizes	min	max	mean	one sample
4	0.65	5.19	1.05	1.19
8	0.61	5.95	1.05	0.77
16	0.59	4.36	1.15	1.11
32	0.56	4.78	0.99	0.74
64	0.77	6.7	1.27	1.16

(B) $e_{l^2}^b$ (%).

TABLE 6. The time-dependent problem (2.25). Prediction's relative l^2 error (4.6) for 150 epochs with different batch sizes on 1000 testing samples: (A) for a homogenized stiffness matrix; (B) for a right-hand side vector of (2.27).

Batch sizes	min	max	mean	one sample
4	1.21	10.93	2.20	2.00
8	1.15	9.54	2.24	1.92
16	0.87	9.11	1.68	1.14
32	0.89	6.84	1.74	1.29
64	0.81	7.16	1.63	1.03

(A) $e_{l^2}^A$ (%).

Batch sizes	min	max	mean	one sample
4	0.54	5.93	0.93	0.84
8	0.58	5.09	0.97	0.83
16	0.48	4.68	0.78	0.68
32	0.51	4.75	0.87	0.58
64	0.47	5.16	0.91	0.47

(B) $e_{l^2}^b$ (%).

TABLE 7. The time-dependent problem (2.25). Prediction's relative l^2 error (4.6) for 300 epochs with different batch sizes on 1000 testing samples: (A) for a homogenized stiffness matrix; (B) for a right-hand side vector of (2.27).

Batch sizes	min	max	mean	one sample
4	1.61	10.9	2.46	2.14
8	0.94	13.87	1.76	1.27
16	1.01	7.08	1.95	1.29
32	0.81	6.81	1.65	0.88
64	0.78	8.55	1.69	0.98

(A) $e_{l^2}^A$ (%).

Batch sizes	min	max	mean	one sample
4	0.61	3.22	1.01	0.93
8	0.55	2.95	0.93	0.66
16	0.48	4.26	0.74	0.56
32	0.51	4.01	0.84	0.55
64	0.51	4.41	0.82	0.56

(B) $e_{l^2}^b$ (%).

TABLE 8. The time-dependent problem (2.25). Prediction's relative l^2 error (4.6) for 600 epochs with different batch sizes on 1000 testing samples: (A) for a homogenized stiffness matrix; (B) for a right-hand side vector of (2.27).

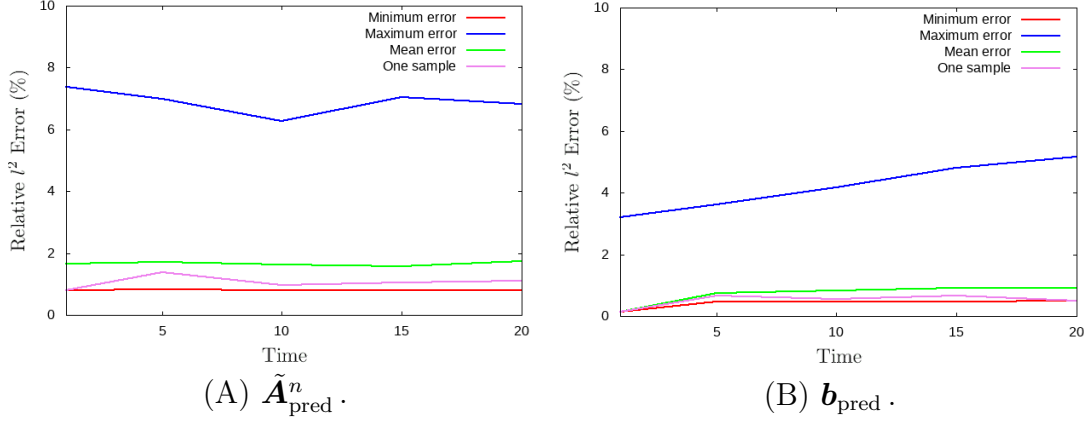


FIGURE 7. The time-dependent problem (2.25). Distribution of prediction's relative l^2 errors (4.6) at several time steps. Those are the min, max, and mean errors as well as one certain sample error: (A) for homogenized stiffness matrix; (B) for right-hand side vector of (2.27).

Now, Fig. 8 shows numerical results for the solution to the homogenized equation of the time-dependent Richards equation (2.25) at the last temporal step, using the first permeability field from Fig. 4: solution p_c to (2.33) is obtained by numerical homogenization, solution $p_{c,\text{pred}}^E$ of (3.11) is achieved by DNN-prediction of effective permeability field, solution $p_{c,\text{pred}}^A$ from (3.11) is reached by DNN-prediction of the coarse-scale homogenized stiffness matrix together with right-hand side vector of (2.27) at the last Picard step.

Then, 1000 test samples are used in numerical experiments. In other words, we compare the homogenized solution p_c (2.33) with the predicted solution in terms of relative L^2 and H^1 errors (4.7). Tables 9 and 10 present the relative L^2 and H^1 errors between p_c (2.33) and $p_{c,\text{pred}}^E$ (3.11) as well as between p_c (2.33) and $p_{c,\text{pred}}^A$ (3.11), respectively. We show mean, minimum, maximum, and one sample errors for the last Picard iteration at the last time step. Figs. 9 and 10 express the distribution of solutions' relative L^2 and H^1 errors over the chosen 5 time steps (1st, 5th, 10th, 15th, 20th).

It is clear from Tables 9 and 10 that the errors' behaviors are similar to the steady-state case (4.9). The only difference is that for the solutions' mean errors, DNN-prediction by homogenized stiffness matrix and right-hand side vector of (2.27) becomes better than DNN-prediction by effective permeability, and this difference is also observable on Figs. 9 and 10. Generally, however, both the approaches (prediction by effective permeability as well as by matrix and vector) provide solutions with small errors. For all cases, errors are smaller than 8%. By accuracy, the mean error distribution is closer to the minimum error than to the maximum error. Note that for this time-dependent case, the approach with prediction of matrix and vector works better than the one with prediction of effective permeability because in applied problems, we need to know solution only at some important temporal points. It is more profitable to get only four or five crucial solutions than to make complex calculations over the entire temporal interval. In summary, the proposed approach has a good accuracy for the time-dependent Richards problem (2.25).

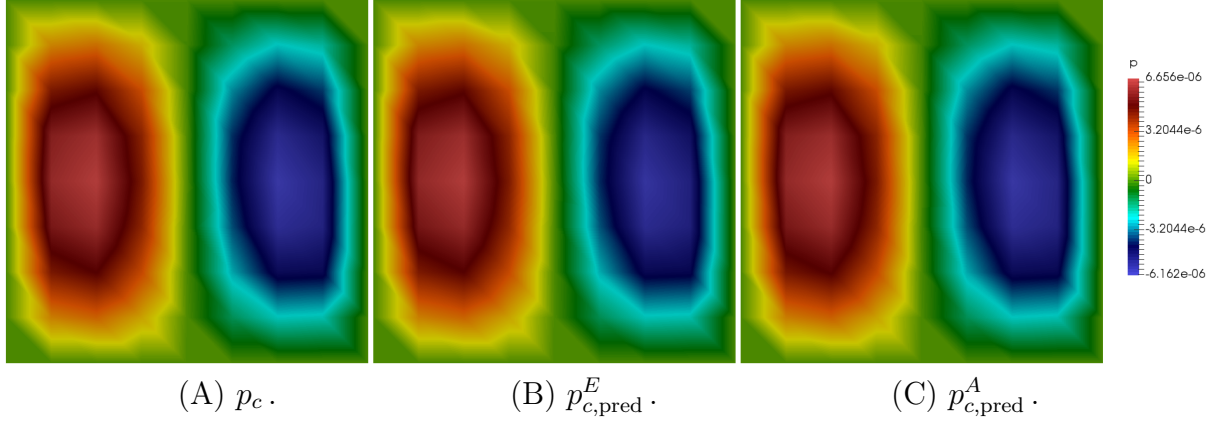


FIGURE 8. The time-dependent problem (2.25). Numerical results for solutions at the last temporal step (using the first permeability field from Fig. 4): (A) homogenized solution; (B) solution obtained by prediction of effective permeability; (C) solution obtained by prediction of the homogenized stiffness matrix and right-hand side vector of (2.27) at the last Picard step.

	$e_{L^2}^E$ (%)	$e_{H^1}^E$ (%)
Mean error	1.469	2.121
Minimum error	0.403	0.781
Maximum error	5.852	6.231
One sample	0.966	1.372

TABLE 9. The time-dependent problem (2.25). Numerical results for solutions at the last time step (the case one sample uses the first permeability field from Fig. 4): relative L^2 and H^1 errors (4.7) between homogenized solution p_c and solution $p_{c,\text{pred}}^E$ obtained by prediction of effective permeability at the last Picard step.

	$e_{L^2}^A$ (%)	$e_{H^1}^A$ (%)
Mean error	0.903	1.843
Minimum error	0.399	1.011
Maximum error	6.649	7.444
One sample	0.607	1.061

TABLE 10. The time-dependent problem (2.25). Numerical results for solutions at the last time step (the case one sample uses the first permeability field from Fig. 4): relative L^2 and H^1 errors (4.7) between homogenized solution p_c and solution $p_{c,\text{pred}}^A$ obtained by prediction of the homogenized stiffness matrix together with right-hand side vector of (2.27) at the last Picard step.

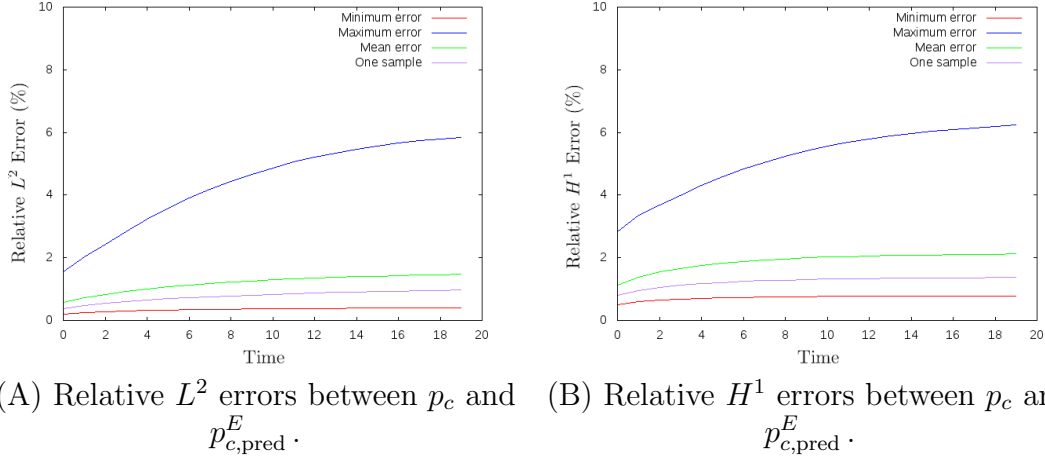


FIGURE 9. The time-dependent problem (2.25). Numerical results for solutions achieved by homogenization and by DNN-prediction of effective permeability (the case one sample uses the first permeability field from Fig. 4): (A) distribution of relative L^2 errors (4.7) by time; (B) distribution of relative H^1 errors (4.7) by time.

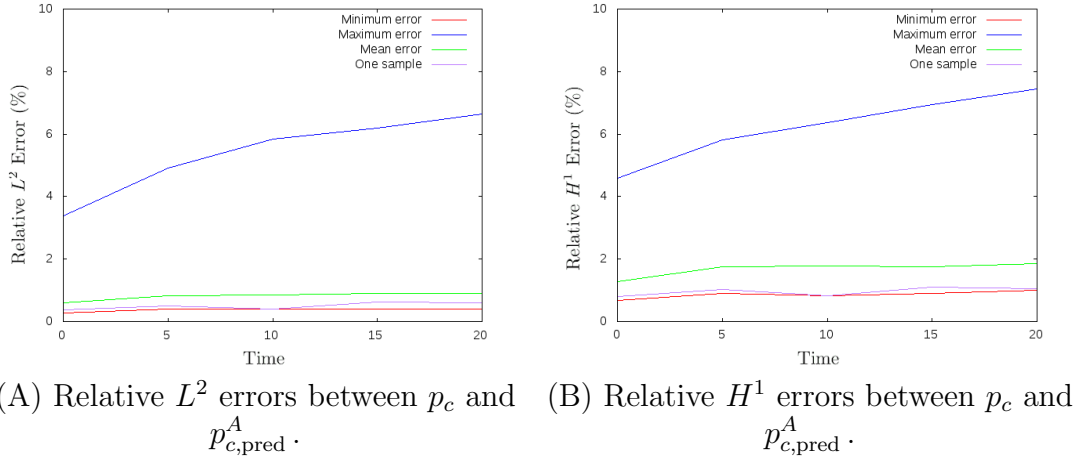


FIGURE 10. The time-dependent problem (2.25). Numerical results for solutions obtained by homogenization and by DNN-prediction of the coarse-scale homogenized stiffness matrix together with right-hand side vector of (2.27) (the case one sample uses the first permeability field from Fig. 4): (A) distribution of relative L^2 errors (4.7) by time; (B) distribution of relative H^1 errors (4.7) by time.

5. CONCLUSIONS

In this paper, we establish a new coarse-grid approximation algorithm for the Richards equation as an unsaturated flow throughout heterogeneous media, utilizing numerical homogenization. Our method takes advantage of deep neural networks (DNN) to swiftly

and repeatedly compute macroscopic parameters. To be more precise, we train neural networks using a training set made up of stochastic permeability realizations and corresponding calculated macroscopic parameters (effective permeability, homogenized stiffness matrix, and right-hand side vector). Our suggested deep learning method creates maps between permeability fields and such macroscopic features, and the handling of Richards equation's nonlinearity is incorporated in the prediction of coarse-scale homogenized stiffness matrix, which is a novelty. Finally, some good numerical results, especially for solutions, are presented to confirm the theory.

Acknowledgements. The reported study was funded by RFBR-VAST under the project number 21-51-54001 and supported by Duy Tan University under decision 5390/QD-DHDT.

APPENDIX A. GLOBAL CONVERGENCE OF PICARD LINEARIZATION PROCEDURE

Consider Eq. (2.2), following [36, 31, 30] (as well as thanks to J. Batista and A. Mazucato, personal communication, January 9, 2022), we will prove the global convergence of Picard linearization process (presented in Subsection 2.2) for the system (2.12) based on (2.7), with $i = 1, 2$. For simplicity, we remove from (2.12) the subscripts H and $(s + 1)$, where Picard iteration steps are applied. Let $\|\cdot\|$ and (\cdot, \cdot) respectively denote the $L^2(\Omega)$ -norm and inner product in $L^2(\Omega)$.

Recall from Assumption (2.3) that the conductivity coefficient κ satisfies $\underline{\kappa} \leq \kappa \leq \overline{\kappa}$, for some constants $\underline{\kappa}, \overline{\kappa} > 0$. Also, (2.4) assumed that $p_0 = p(0, \mathbf{x}) \in V = H_0^1(\Omega)$. Without confusion, now $\kappa(\mathbf{x}, p)$ is denoted by $\kappa(p)$. An additional assumption on $\kappa(\mathbf{x}, \cdot)$ is the Lipschitz continuity as follows.

Assumption A.1. *There exists $L_\kappa > 0$ (without any explicit dependence on \mathbf{x} and t) such that for all $\mathbf{x} \in \Omega$ and $p_1, p_2 \in V$,*

$$(A.1) \quad |\kappa(p_1) - \kappa(p_2)| \leq L_\kappa |p_1 - p_2|.$$

By Poincaré inequality, there exists a constant C_Ω depending only on Ω such that

$$(A.2) \quad \|p^{n+1} - p_{s+1}\| \leq C_\Omega \|\nabla(p^{n+1} - p_{s+1})\|,$$

Also, assume that $p_{s+1}(t, \cdot) \in C_c^\infty(\Omega)$ so that $\|p_{s+1}\|_\infty \leq \hat{D} \|\nabla p_{s+1}\|_\infty$, where \hat{D} is the distance between the two parallel hyperplanes bounding Ω . Let U be the exact solution of the equation at hand (2.2). Then, we obtain the following inequalities by applying the error estimate in [44] (Theorem 1.5):

$$(A.3) \quad \begin{aligned} \frac{1}{\hat{D}} \|p_{s+1}\|_\infty &\leq \|\nabla p_{s+1}\|_\infty \leq \|\nabla(p_{s+1} - U(t_{s+1}))\|_\infty + \|\nabla U(t_{s+1})\|_\infty \\ &\leq \overline{C}(U)(H + \tau) + \|\nabla U(t_{s+1})\|_\infty = M, \end{aligned}$$

for some constant $\overline{C}(U)$ depending on U .

Then in V^H , we get the following equality by subtracting (2.7) from (2.12) and picking correct $v = p^{n+1} - p_{s+1}$:

$$(A.4) \quad \frac{1}{\tau} \|p^{n+1} - p_{s+1}\|^2 + a(p^{n+1}, p^{n+1} - p_{s+1}; p^n) = a(p_{s+1}, p^{n+1} - p_{s+1}; p_{s+1}).$$

Equivalently,

$$(A.5) \quad \begin{aligned} & \|p^{n+1} - p_{s+1}\|^2 + \tau(\chi(p^n) \nabla(p^{n+1} - p_{s+1}), \nabla(p^{n+1} - p_{s+1})) \\ & = -\tau((\chi(p^n) - \chi(p_{s+1})) \nabla p_{s+1}, \nabla(p^{n+1} - p_{s+1})). \end{aligned}$$

Using Assumption (2.3) for the left-hand side of (A.5), then Cauchy-Schwarz inequality, Assumption (A.1), and the Young's inequality for the right-hand side of (A.5), we achieve

$$(A.6) \quad \begin{aligned} \|p^{n+1} - p_{s+1}\|^2 + \tau \underline{\chi} \|\nabla(p^{n+1} - p_{s+1})\|^2 & \leq \frac{\tau L_\chi^2}{2 \underline{\chi}} \|\nabla p_{s+1}\|_\infty^2 \|p^n - p_{s+1}\|^2 \\ & + \frac{\tau \underline{\chi}}{2} \|\nabla(p^{n+1} - p_{s+1})\|^2. \end{aligned}$$

Employing (A.3) and (A.2), we derive from (A.6) that

$$(A.7) \quad \left(1 + \frac{\tau \underline{\chi}}{2 C_\Omega^2}\right) \|p^{n+1} - p_{s+1}\|^2 \leq \frac{\tau L_\chi^2 M^2}{2 \underline{\chi}} \|p^n - p_{s+1}\|^2,$$

and thus,

$$(A.8) \quad \|p^{n+1} - p_{s+1}\|^2 \leq \frac{C L_\chi^2}{2 \underline{\chi}} \frac{\tau}{1 + \frac{\tau \underline{\chi}}{2 C_\Omega^2}} (\tilde{C}(H + \tau) + 1)^2 \|p^n - p_{s+1}\|^2 := \lambda \|p^n - p_{s+1}\|^2,$$

for some positive constants C, \tilde{C} . With sufficiently small τ and H , the coefficient λ will be less than 1, implying that the algorithm converges. Specifically, $\lambda \rightarrow 0$ when $H \rightarrow 0$ and $\tau \rightarrow 0$ at the same time.

Similar proof holds for Eq. (2.25) and its homogenized Eq. (2.26) having discretization (2.27).

REFERENCES

- [1] J. E. Aarnes and Y. Efendiev. [Mixed multiscale finite element methods for stochastic porous media flows](#). *SIAM Journal on Scientific Computing*, 30(5):2319–2339, 2008.
- [2] R. G. Baca, R. C. Arnett, and D. W. Langford. [Modelling fluid flow in fractured-porous rock masses by finite-element techniques](#). *International Journal for Numerical Methods in Fluids*, 4(4):337–348, 1984.
- [3] Michael A. Celia and Philip Binning. [A mass conservative numerical solution for two-phase flow in porous media with application to unsaturated flow](#). *Water Resources Research*, 28(10):2819–2828, 1992.
- [4] Michael A. Celia, Efthimios T. Bouloutas, and Rebecca L. Zarba. [A general mass-conservative numerical solution for the unsaturated flow equation](#). *Water Resources Research*, 26(7):1483–1496, 1990.
- [5] Zhiming Chen, Weibing Deng, and Huang Ye. [Upscaling of a class of nonlinear parabolic equations for the flow transport in heterogeneous porous media](#). *Commun. Math. Sci.*, 3(4):493–515, 2005.
- [6] Siu Wun Cheung, Eric T. Chung, Yalchin Efendiev, Eduardo Gildin, Yating Wang, and Jingyan Zhang. [Deep global model reduction learning in porous media flow simulation](#). *Computational Geosciences*, 24(1):261–274, 2020.

- [7] François Chollet. Keras, 2015. Available online: <https://keras.io/> (accessed on 6 June 2022).
- [8] G. Cybenko. [Approximation by superpositions of a sigmoidal function](#). *Mathematics of Control, Signals and Systems*, 2(4):303–314, 1989.
- [9] P. Dostert, Y. Efendiev, and B. Mohanty. [Efficient uncertainty quantification techniques in inverse problems for Richards’ equation using coarse-scale simulation models](#). *Advances in Water Resources*, 32(3):329–339, 2009.
- [10] Louis J. Durlofsky. [Numerical calculation of equivalent grid block permeability tensors for heterogeneous porous media](#). *Water Resources Research*, 27(5):699–708, 1991.
- [11] Yalchin Efendiev and Wing Tat Leung. [Multicontinuum homogenization and its relation to nonlocal multicontinuum theories](#), 2022. arXiv:2208.04005.
- [12] Yalchin Efendiev, Wing Tat Leung, Wenyuan Li, and Zecheng Zhang. [Hybrid explicit-implicit learning for multiscale problems with time dependent source](#), 2022. arXiv:2208.06790.
- [13] Matthew W. Farthing and Fred L. Ogden. [Numerical solution of Richards’ equation: A review of advances and challenges](#). *Soil Science Society of America Journal*, 81(6):1257–1269, 2017.
- [14] Shubin Fu, Eric Chung, and Tina Mai. [Constraint energy minimizing generalized multiscale finite element method for nonlinear poroelasticity and elasticity](#). *Journal of Computational Physics*, 417:109569, 2020.
- [15] Benjamin Ganis, Hector Klie, Mary F. Wheeler, Tim Wildey, Ivan Yotov, and Dongxiao Zhang. [Stochastic collocation and mixed finite elements for flow in porous media](#). *Computer methods in applied mechanics and engineering*, 197(43-44):3547–3559, 2008.
- [16] Xavier Glorot, Antoine Bordes, and Yoshua Bengio. [Deep sparse rectifier neural networks](#). In Geoffrey Gordon, David Dunson, and Miroslav Dudík, editors, *Proceedings of the Fourteenth International Conference on Artificial Intelligence and Statistics*, volume 15 of *Proceedings of Machine Learning Research*, pages 315–323, Fort Lauderdale, FL, USA, 11–13 Apr 2011. PMLR.
- [17] Ian Goodfellow, Yoshua Bengio, and Aaron Courville. *Deep Learning*. MIT Press, 2016. <http://www.deeplearningbook.org>.
- [18] Boris Hanin. [Universal function approximation by deep neural nets with bounded width and ReLU activations](#). *Mathematics*, 7(10):992-1–992-9, 2019.
- [19] R. Haverkamp, M. Vauclin, J. Touma, P. J. Wierenga, and G. Vachaud. [A comparison of numerical simulation models for one-dimensional infiltration](#). *Soil Science Society of America Journal*, 41(2):285–294, 1977.
- [20] Kaiming He, Xiangyu Zhang, Shaoqing Ren, and Jian Sun. [Deep residual learning for image recognition](#). In *2016 IEEE Conference on Computer Vision and Pattern Recognition (CVPR)*, pages 770–778, 2016.
- [21] Xinguang He and Li Ren. [An adaptive multiscale finite element method for unsaturated flow problems in heterogeneous porous media](#). *Journal of Hydrology*, 374(1):56 – 70, 2009.
- [22] Philip Heger, Markus Full, Daniel Hilger, and Norbert Hosters. [Investigation of physics-informed deep learning for the prediction of parametric, three-dimensional](#)

- flow based on boundary data, 2022. arXiv:2203.09204.
- [23] Geoffrey Hinton, Li Deng, Dong Yu, George E. Dahl, Abdel-rahman Mohamed, Navdeep Jaitly, Andrew Senior, Vincent Vanhoucke, Patrick Nguyen, Tara N. Sainath, and Brian Kingsbury. [Deep neural networks for acoustic modeling in speech recognition: The shared views of four research groups](#). *IEEE Signal Processing Magazine*, 29(6):82–97, 2012.
 - [24] Kurt Hornik. [Approximation capabilities of multilayer feedforward networks](#). *Neural Networks*, 4(2):251–257, 1991.
 - [25] Diederik P. Kingma and Jimmy Ba. [Adam: A method for stochastic optimization](#), 2014. arXiv:1412.6980.
 - [26] Günter Klambauer, Thomas Unterthiner, Andreas Mayr, and Sepp Hochreiter. [Self-normalizing neural networks](#), 2017. arXiv:1706.02515.
 - [27] Alex Krizhevsky, Ilya Sutskever, and Geoffrey E. Hinton. [ImageNet classification with deep convolutional neural networks](#). *Commun. ACM*, 60(6):84–90, May 2017.
 - [28] Yann LeCun, Yoshua Bengio, and Geoffrey Hinton. [Deep learning](#). *Nature*, 521(7553):436–444, May 2015.
 - [29] Na Li, Li Ren, and Xingye Yue. [Application and validation of an upscaling method for unsaturated water flow processes in heterogeneous soils](#). *Vadose Zone Journal*, 14(7):1–23, 2015.
 - [30] Florian List and Florin A. Radu. [A study on iterative methods for solving Richards’ equation](#). *Computational Geosciences*, 20(2):341–353, Apr 2016.
 - [31] Anotida Madzvamuse and Andy H.W. Chung. [Fully implicit time-stepping schemes and non-linear solvers for systems of reaction-diffusion equations](#). *Applied Mathematics and Computation*, 244:361–374, 2014.
 - [32] Tina Mai, Siu Wun Cheung, and Jun Sur Richard Park. [Constraint energy minimizing generalized multiscale finite element method for multi-continuum Richards equations](#), 2022. arXiv:2205.11294.
 - [33] Tina Mai and Daniele Mortari. [Theory of functional connections applied to quadratic and nonlinear programming under equality constraints](#). *Journal of Computational and Applied Mathematics*, 406:113912, 2022.
 - [34] Hrushikesh Mhaskar, Qianli Liao, and Tomaso Poggio. [Learning functions: When is deep better than shallow](#), 2016. arXiv:1603.00988.
 - [35] J.R. Nimmo. [Vadose Water](#). In Gene E. Likens, editor, *Encyclopedia of Inland Waters*, pages 766–777. Academic Press, Oxford, 2009.
 - [36] Jun Sur Richard Park, Siu Wun Cheung, and Tina Mai. [Multiscale simulations for multi-continuum Richards equations](#). *Journal of Computational and Applied Mathematics*, 397:113648, 2021.
 - [37] Jun Sur Richard Park, Siu Wun Cheung, Tina Mai, and Viet Ha Hoang. [Multi-scale simulations for upscaled multi-continuum flows](#). *Journal of Computational and Applied Mathematics*, 374:112782, 2020.
 - [38] Jun Sur Richard Park and Viet Ha Hoang. [Homogenization of a multiscale multi-continuum system](#). *Applicable Analysis*, 101(4):1271–1298, 2022.

- [39] Jun Sur Richard Park and Xueyu Zhu. [Physics-informed neural networks for learning the homogenized coefficients of multiscale elliptic equations](#). *Journal of Computational Physics*, 467:111420, 2022.
- [40] L. A. Richards. [Capillary conduction of liquids through porous mediums](#). *Physics*, 1(5):318–333, 1931.
- [41] J. Skopp. Class notes: Physical concepts of soils. University of Nebraska, Lincoln, Nebraska, 1994.
- [42] Denis Spiridonov, Maria Vasilyeva, and Eric T. Chung. [Generalized multiscale finite element method for multicontinua unsaturated flow problems in fractured porous media](#). *Journal of Computational and Applied Mathematics*, 370:112594, 2020.
- [43] Matus Telgarsky. [Benefits of depth in neural networks](#), 2016. arXiv:1602.04485.
- [44] V. Thomée. *Galerkin Finite Element Methods for Parabolic Problems*, volume 25 of *Springer Series in Computational Mathematics*. Springer-Verlag Berlin Heidelberg, second edition, 2006.
- [45] A Tyrylgina, D Spiridonov, and M Vasilyeva. [Numerical homogenization for poroelasticity problem in heterogeneous media](#). *Journal of Physics: Conference Series*, 1158:042030, 2019.
- [46] M Vasilyeva and A Tyrylgina. [Convolutional neural network for fast prediction of the effective properties of domains with random inclusions](#). *Journal of Physics: Conference Series*, 1158:042034, 2019.
- [47] Maria Vasilyeva, Wing T. Leung, Eric T. Chung, Yalchin Efendiev, and Mary Wheeler. [Learning macroscopic parameters in nonlinear multiscale simulations using nonlocal multicontinua upscaling techniques](#). *Journal of Computational Physics*, 412:109323, 2020.
- [48] Maria Vasilyeva, Aleksei Tyrylgina, Donald L. Brown, and Anirban Mondal. [Preconditioning Markov Chain Monte Carlo Method for Geomechanical Subsidence using multiscale method and machine learning technique](#). *Journal of Computational and Applied Mathematics*, 392:113420, 2021.
- [49] Maria Vasilyeva and Aleksey Tyrylgina. [Machine learning for accelerating macroscopic parameters prediction for poroelasticity problem in stochastic media](#). *Computers & Mathematics with Applications*, 84:185–202, 2021.
- [50] Flora Chu Wang, Nabil A. Hassan, and Joseph B. Franzini. [A method of analyzing unsteady, unsaturated flow in soils](#). *Journal of Geophysical Research (1896-1977)*, 69(12):2569–2577, 1964.
- [51] Min Wang, Siu Wun Cheung, Eric T. Chung, Yalchin Efendiev, Wing Tat Leung, and Yating Wang. [Prediction of discretization of GMsFEM using deep learning](#). *Mathematics*, 7(5):412–1–412–16, 2019.
- [52] Min Wang, Siu Wun Cheung, Wing Tat Leung, Eric T Chung, Yalchin Efendiev, and Mary Wheeler. [Reduced-order deep learning for flow dynamics. The interplay between deep learning and model reduction](#). *Journal of Computational Physics*, 401:108939, 2020.
- [53] Yating Wang, Siu Wun Cheung, Eric T Chung, Yalchin Efendiev, and Min Wang. [Deep multiscale model learning](#). *Journal of Computational Physics*, 406:109071, 2020.

- [54] Colby L. Wight and Jia Zhao. [Solving Allen-Cahn and Cahn-Hilliard equations using the adaptive physics informed neural networks](#). *Communications in Computational Physics*, 29(3):930–954, 2021.
- [55] E. Wong. *Stochastic Processes in Information and Dynamical Systems*. McGraw-Hill, New York, 1971.
- [56] X.H. Wu, Y. Efendiev, and Thomas Y. Hou. [Analysis of upscaling absolute permeability](#). *Discrete and Continuous Dynamical Systems - B*, 2(2):185–204, 2002.
- [57] Lei Yuan, Yi-Qing Ni, Xiang-Yun Deng, and Shuo Hao. [A-PINN: Auxiliary physics informed neural networks for forward and inverse problems of nonlinear integro-differential equations](#). *Journal of Computational Physics*, 462:111260, 2022.